NEUROSCIENCE

Single-synapse analyses of Alzheimer's disease implicate pathologic tau, DJ1, CD47, and ApoE

Thanaphong Phongpreecha[1,2,3]†, Chandresh R. Gajera[1]†, Candace C. Liu[1], Kausalia Vijayaragavan[1], Alan L. Chang[2,3,4], Martin Becker[2,3,4], Ramin Fallahzadeh[2,3,4], Rosemary Fernandez[1], Nadia Postupna[5], Emily Sherfield[5], Dmitry Tebaykin[1], Caitlin Latimer[5], Carol A. Shively[6], Thomas C. Register[6], Suzanne Craft[7], Kathleen S. Montine[1], Edward J. Fox[1], Kathleen L. Poston[8,9], C. Dirk Keene[5], Michael Angelo[1], Sean C. Bendall[1], Nima Aghaeepour[2,3,4], Thomas J. Montine[1]*

Synaptic molecular characterization is limited for Alzheimer's disease (AD). Our newly invented mass cytometry–based method, synaptometry by time of flight (SynTOF), was used to measure 38 antibody probes in approximately 17 million single-synapse events from human brains without pathologic change or with pure AD or Lewy body disease (LBD), nonhuman primates (NHPs), and PS/APP mice. Synaptic molecular integrity in humans and NHP was similar. Although not detected in human synapses, Aβ was in PS/APP mice single-synapse events. Clustering and pattern identification of human synapses showed expected disease-specific differences, like increased hippocampal pathologic tau in AD and reduced caudate dopamine transporter in LBD, and revealed previously unidentified findings including increased hippocampal CD47 and lowered DJ1 in AD and higher ApoE in AD with dementia. Our results were independently supported by multiplex ion beam imaging of intact tissue. This highlights the higher depth and breadth of insight on neurodegenerative diseases obtainable through SynTOF.

INTRODUCTION

The anatomical basis of cognitive impairment in Alzheimer's disease (AD) is loss of limbic and neocortical synapses. This is supported by ultrastructural and microscopic studies that assessed hundreds of human synapses but with limited molecular characterization, and by molecular characterization of bulk preparations of synaptic particles from specialized brain homogenates called synaptosomes (*1*–*12*).

More recently, array tomography (three to five antibodies) and conventional flow cytometry (two to four antibodies) have characterized hundreds of thousands to a million individual human single-synapse events from synaptosome preparations (*13*–*15*). SynTOF (synaptometry by time of flight) (*16*, *17*) quantifies tens of millions of individual single-synapse events by mass cytometry, permitting robust machine learning (ML) applications. Here, we performed SynTOF on synaptosome preparations from healthy nonhuman primates (NHPs), PS/APP mice, and postmortem tissue from carefully selected individuals with only AD neuropathologic change (ADNC) (*18*, *19*) or only Lewy body disease (LBD) (*18*, *19*), as well as from normal age-matched adults. We tested the hypothesis that the synaptic molecular composition in humans with only AD resembled aged PS/APP mice, one of the most widely used transgenic models of AD. We then used ML approaches to identify presynaptic subpopulations in controls and to discover previously unidentified disease-related changes in synaptic molecular composition. Last, we confirmed the major features of ML-identified synaptic subpopulations with multiplexed ion beam imaging (MIBI).

[1]Department of Pathology, Stanford University, Stanford, CA, USA. [2]Department of Anesthesiology, Perioperative, and Pain Medicine, Stanford University, Stanford, CA, USA. [3]Department of Biomedical Data Science, Stanford University, Stanford, CA, USA. [4]Department of Pediatrics, Stanford University, Stanford, CA, USA. [5]Department of Pathology, University of Washington, Seattle, WA, USA. [6]Department of Pathology/Comparative Medicine, Wake Forest School of Medicine, Winston-Salem, NC, USA. [7]Department of Internal Medicine–Geriatrics, Wake Forest School of Medicine, Winston-Salem, NC, USA. [8]Department of Neurology and Neurological Sciences, Stanford University, Stanford, CA, USA. [9]Department of Neurosurgery, Stanford University, Stanford, CA, USA.
*Corresponding author. Email: tmontine@stanford.edu
†These authors contributed equally to this work.

RESULTS

Generation of single-synapse data via SynTOF

Over a 5-year period, 113 synaptosome preparations were prospectively cryopreserved from all postmortem human brains collected from carefully annotated adult research participants. A relatively small number were of exceptionally high quality because of their short postmortem interval and pathologic confirmation as no or only one type of histopathologic change. Specifically, 21 met rigorous inclusion/exclusion criteria for both clinical and pathologic features: Controls ($n = 6$), high-level ADNC only ($n = 9$), and high-level LBD only ($n = 6$) (table S1); note that the ADNC and LBD groups each contained two resilient individuals, meaning high-level pathologic change without clinical diagnosis of dementia and/or Parkinson's disease (PD) (*20*). Following our established protocol (*17*) (see Materials and Methods), samples were prepared, barcoded, stained with a 38-plex SynTOF panel (shown in Fig. 1 and table S2), and analyzed by mass cytometry. Similar analysis was performed on NHP tissue controls and PS/APP transgenic mice (see Materials and Methods). Together, these approximately 17 million single synaptic events comprise the data analyzed.

Pseudo-bulk analysis of human and mouse single-synapse events

The first goal was to analyze the data by established gating protocols (*16*, *17*) to facilitate comparison with existing human data obtained using other technologies, and to compare across species. Expected regional variation was observed in Control presynaptic events (Fig. 1A), including reciprocal variation in average glutamatergic ($P < 0.01$) and GABAergic ($P < 0.05$) events between Brodmann area 9 (BA9)

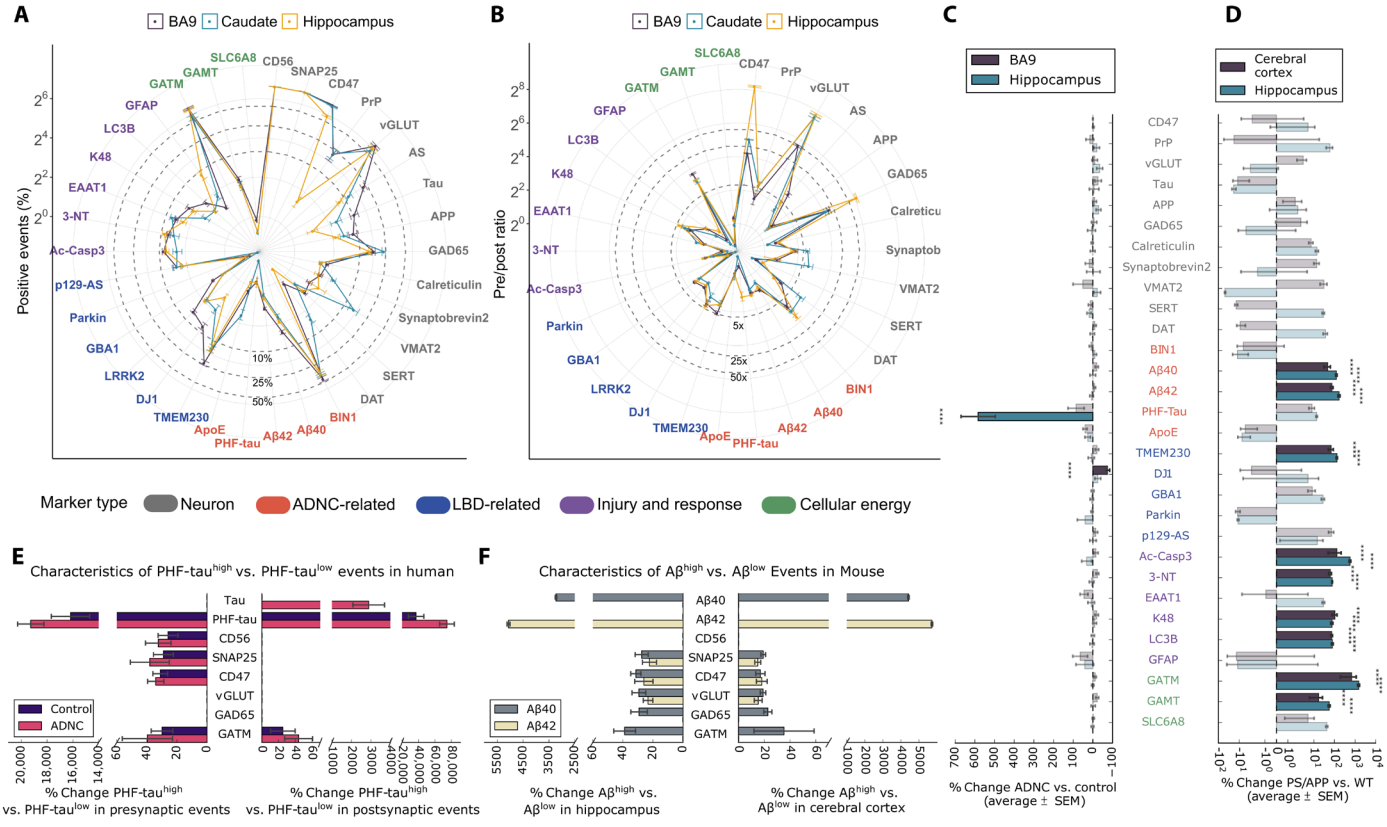

Fig. 1. SynTOF panel results for human and mouse synaptosomes analyzed as average % positive events (±SEM). Our 38-antibody panel comprises the 30 antibodies listed in (C) plus six gating antibodies (CD11b, MBP, CD56, SNAP25, PSD95, and gephyrin) plus two antibodies (AS and LRRK2) that did not label both human and mouse tissue. See table S2 for additional information, including how these antibodies were grouped into marker types that identify features such as cell type, synapse type, AD, or PD risk gene protein products. In all panels, font color for each antibody indicates which marker type it belongs to: neuron (gray), ADNC-related (red), LBD-related (blue), injury and response (magenta), and cellular energy (green). (**A**) Spider plot of % positive events from BA9, caudate nucleus, and hippocampus from human Control ($n = 6$). (**B**) Spider plot of presynaptic/postsynaptic event ratios for nonzero postsynaptic markers. (**C**) Presynaptic average % change in % positive events (±SEM) in BA9, caudate, and hippocampus from human Control, ADNC ($n = 9$), and LBD ($n = 6$) analyzed by two-way analysis of variance (ANOVA) with brain region versus diagnostic group. The bars in bold colors with asterisks present the results with significant differences ($P < 0.001$). Results for LBD samples are presented in text. (**D**) Similar to (C) but for cerebral cortical and hippocampal presynaptic results from 22-month-old PS/APP ($n = 5$) versus WT ($n = 5$) mice. (**E**) Hippocampus presynaptic and postsynaptic % change in mean intensity (±SEM) in both Control and ADNC samples analyzed by two-way ANOVA with PHF-tau^{high} or PHF-tau^{low} versus mean intensity for each probe. Only significantly greater mean intensity following correction for multiple comparisons is presented. (**F**) Similar to (E) but for hippocampus or cerebral cortex presynaptic events in PS/APP mice divided into Aβ40^{high} versus Aβ40^{low} events or Aβ42^{high} versus Aβ42^{low} events.

and caudate, and greater % dopamine transporter (DAT)–positive presynaptic events in caudate versus BA9 ($P < 0.001$) or versus hippocampus ($P < 0.001$; fig. S1) (*21*–*26*). The pre-/postsynaptic ratio in Controls for proteins known to be enriched in the presynaptic fraction ranged from 5- to >200-fold (Fig. 1B). These results support previous work that showed that human synaptosomes prepared using our protocol have the expected enrichment in neuronal markers and membrane-bound bodies that contain synaptic vesicles compared to Western blots and transmission electron microscopy. That our synaptosome preparations are permeabilized to allow access of antibodies to intracellular epitopes was validated by the excellent agreement between our estimates, using antibodies to intracellular targets, of pre–single-synapse (SNAP25) versus post–single-synapse (PSD95) events, as well as by our estimates of brain regional fraction of excitatory (vGLUT), inhibitory (GAD), and dopaminergic (VMAT) synapses compared with those made by transmission electron microscopy (fig. S1). By SynTOF, presynaptic average % positive events were 4.3 ± 0.4% and 2.0 ± 0.2% for $A\beta_{40}$ and $A\beta_{42}$, respectively, in BA9 and 18.1 ± 1.7% for paired-helical-filament (PHF)–tau in hippocampus for ADNC; these results align well with 0.6 to 5.1% Aβ-positive (*13*) and 15.4% pathologic tau–positive (*15*) events in presynaptic synaptosomes in AD by array tomography. Our results demonstrate that human SynTOF data derive from synaptic preparations with high molecular integrity, show expected patterns of anatomical distribution, and compare well with data collected by others using transmission electron microscopy or array tomography.

Presynaptic average % positive events for two antibody probes were significantly different ($P < 0.001$) when comparing ADNC to Controls: hippocampus had more PHF-tau (525%) and BA9 had less DJ1 (49%) (Fig. 1C). LBD was significantly different from Control only for 51% reduction in caudate DAT^{high} presynaptic events ($P < 0.001$), aligning closely with estimates from biochemical studies and single-photon emission computerized tomography imaging (*27*). Lack of significant presynaptic changes in LBD BA9 and hippocampus

underscored that the changes in AD were disease-specific and not merely covariates of neurodegeneration or dementia such as debilitation or reduced mobility. Although previous studies identified an approximately 20% increase in p129-α-synuclein–positive presynaptic synaptosome preparations in cingulate gyrus and putamen from LBD samples (*14*), we did not observe this in the three regions analyzed here. Postsynaptic average % positive PHF-tau was also significantly increased in ADNC hippocampus compared to Controls ($P < 0.0001$, % change = 320 ± 51), again in agreement with array tomography (*15*).

We tested the hypothesis that Aβ-bearing presynaptic events could be detected by SynTOF by using a common transgenic mouse model of AD. Cerebral cortical and hippocampal synaptosome preparations from 22-month-old wild-type (WT; $n = 5$) and PS/APP ($n = 5$) mice were analyzed by SynTOF exactly as above. Eleven antibodies had significantly increased presynaptic average % positive events in PS/APP compared to WT mice ($P < 0.001$; Fig. 1D); no antibody's signal was significantly decreased. By SynTOF, aged PS/APP mice had approximately 100-fold increase in presynaptic Aβ accumulation as well as many of the responses to Aβ-induced injury that have been reported previously in bulk tissue from AD transgenic mouse models, including increased ubiquitin conjugation (K48), lysosomal stress (LC3B), increased free radical injury (3NT), activated apoptotic signaling (Ac-Casp3), and cellular energy stress as indicated by significantly increased presynaptic expression of the two enzymes that catalyze creatine synthesis (GATM and GAMT; Fig. 1D) (*28*, *29*). An unexpected finding was increased transgenic mouse presynaptic TMEM230, a protein product of a PD risk gene, in aged PS/APP mice.

Human hippocampus presynaptic PHF-tau^{high} events, whether from ADNC (both dementia and resilient) or Control, yielded similar results indicating a stress response to neurofibrillary change independent of clinical status. This included increased capacity to synthesize creatinine in both pre- and postsynaptic events, as well as increased expression of multiple presynaptic proteins, including CD56 and CD47, perhaps as attempts to forestall degeneration (Fig. 1E). Human hippocampus PHF-tau^{high} postsynaptic events again had increased expression of GAMT in Controls and ADNC, and increased tau expression only in ADNC, perhaps indicating an attempt to mitigate sequestration of pathologic tau. Hippocampus and cerebral cortex presynaptic events from aged PS/APP mice were divided into $A\beta_{42}^{high}$ versus $A\beta_{42}^{low}$ or $A\beta_{40}^{high}$ versus $A\beta_{40}^{low}$ events (there were too few postsynaptic events to analyze confidently), and mean intensity of each antibody was analyzed (Fig. 1F). $A\beta_{42}^{high}$ and $A\beta_{40}^{high}$ events were largely distinct populations. In each region, both $A\beta_{42}^{high}$ and $A\beta_{40}^{high}$ events showed significantly increased ($P < 0.001$) expression of vGLUT, SNAP25, and GATM, with the exception of cortical $A\beta_{42}^{high}$ (Fig. 1F). $A\beta_{40}^{high}$ presynaptic events tended to have higher GAD65 expression in both regions ($P < 0.01$). Therefore, pseudo-bulk analyses validated SynTOF data by close agreement with results obtained by other methods in humans and transgenic mice.

Identification of subpopulations from human presynaptic events

We adopted a clustering algorithm based on modified autoencoder (AE) neural networks to identify subpopulations from single-synapse events. Briefly, the AE was used to learn compressed hidden representations of the single-synapse data, and then a *k*-mean–based soft clustering layer was appended and trained with AE to cluster the compressed representation. Using a subset of 24 designated phenotypic markers that did not include disease-specific markers (table S2), the modified AE clustered Control single-presynaptic events from all three brain regions into 15 different subpopulations (see details in Materials and Methods). Figure 2A shows each subpopulation's standardized mean expression for each antibody in all brain regions for Control samples; these characteristics remained similar when stratified by brain region (fig. S2). Subpopulation A comprised two "high-expresser" subpopulations (A1 and A2) with high signals from most antibodies. In contrast, subpopulation B contained two subpopulations (B1 and B2) with low signal from most antibodies, with the exception of GATM and GAMT. Subpopulation C's 11 subpopulations were heterogeneous; C1 to C5 tended to have moderately higher antibody signals than C6 to C11. Several C subpopulations had unique features, e.g., C3 and C6 were GAD65^{high}, C4 was PrP^{high}, C8 was VGLUT^{high}, and C10 was GAMT^{high}. These characteristics are similarly reflected in the 10 pathologic marker profiles of each subpopulation. Markers were highest in A subpopulations and lowest in B subpopulations (Fig. 2A). Note that pathologic markers were not used as a part of AE clustering input, but were calculated post-clustering. Single-presynaptic event data visualized by t-distributed stochastic neighbor embedding (t-SNE) dimensionality reduction showed proximity among subpopulations (Fig. 2B), and their characteristics were appreciated by individual phenotypic marker expressions (fig. S3). In particular, the presynaptic markers CD47 and SNAP25 both showed similar profiles with intermediate to high expression across all subpopulations except subpopulation B (Fig. 2C). Subpopulations C3 and C6 were GAD65^{high}, a traditional marker for synaptic particles from inhibitory neurons, while subpopulations A1, A2, C1, and C8 likely were from excitatory neurons as they exhibited higher VGLUT expression Fig. 2C. Select subpopulations, such as BA9's A1, B1, and C4, are shown (fig. S4) by density plots from a two-step gating strategy optimized by GateFinder (*30*).

Subpopulation frequency varied significantly across brain regions ($P < 0.0001$; Fig. 2D and fig. S5, A to C). BA9 was similar to caudate in most subpopulations, while hippocampus tended to be different from the other two regions. Corrected multiple comparisons revealed significantly ($P < 0.01$) different patterns of regional subpopulation frequencies: BA9 was different from caudate in B2, C2, C6, and C11; BA9 was different from hippocampus in A1, B1, B2, C1 to C5, C7, C9, and C10; and caudate was different from hippocampus in A1, A2, B1, C1, and C3 to C11. These results show a relatively distinct frequency of Control presynaptic subpopulations in the human hippocampus. Because B-type subpopulations were the most frequent in hippocampus, our results suggest that B subpopulations were mostly undifferentiated based on our selected antibody panel and that further refinement of our SynTOF panel may be needed to reflect more fully hippocampus presynaptic diversity. Subpopulation frequencies between Control and the two disease groups were highly correlated (Spearman's $R = 0.89$ for Controls versus ADNC and 0.94 versus LBD) (Fig. 2E), indicating that subpopulation frequency was largely preserved among the three groups (fig. S5, A to C) and suggesting that marker expression rather than frequency alone is important to subpopulation clustering.

Presynaptic subpopulations confirmed pseudo-bulk findings and revealed additional strong signals from ADNC and LBD presynaptic events

On the basis of the subpopulations identified in Fig. 2A, we next focused on using conventional ML to identify regional differences in

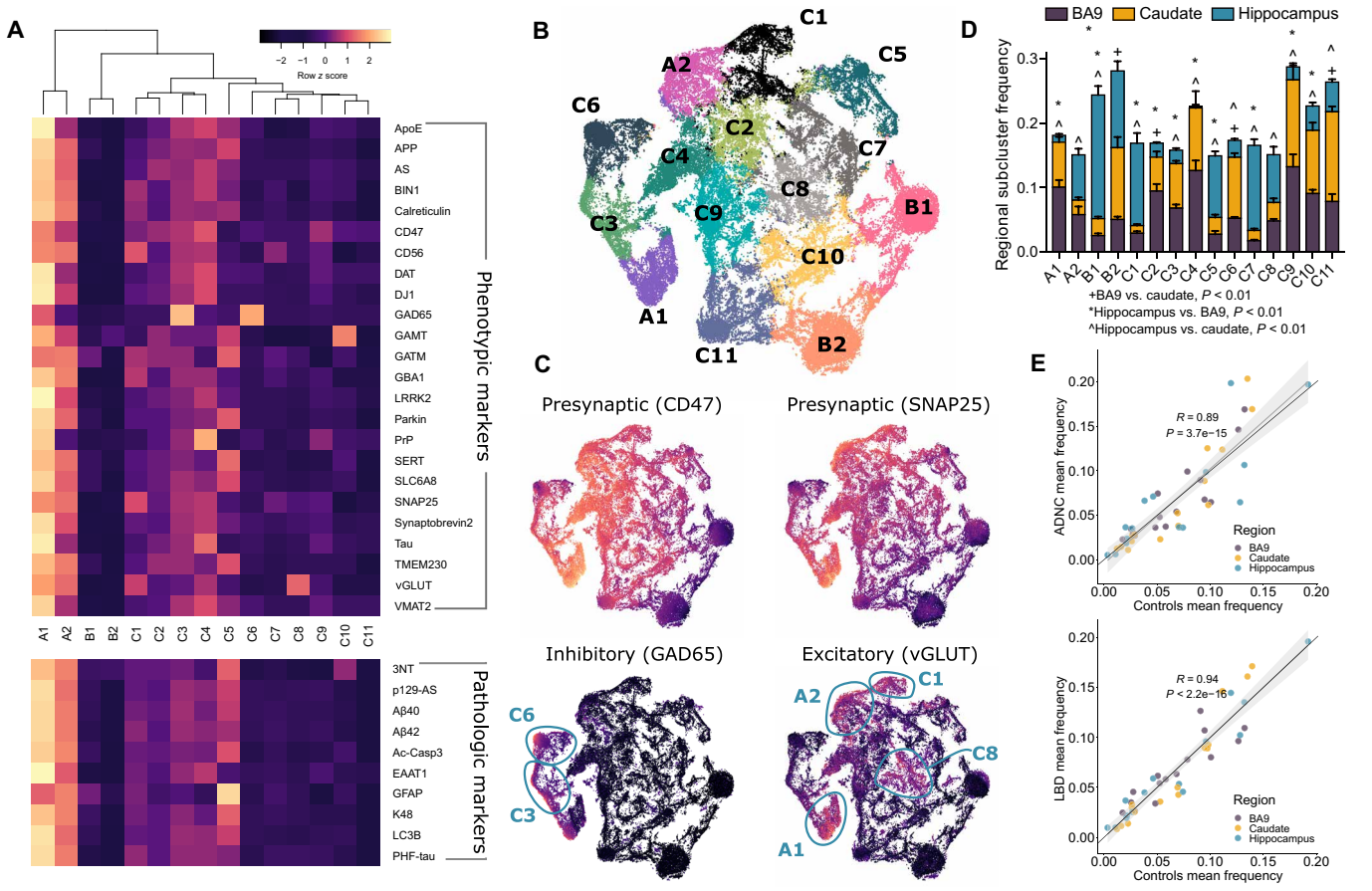

Fig. 2. The modified deep AE clustered Control sample presynaptic events into different phenotypic marker–based subpopulations. (**A**) Heatmap showing the mean expression values from Control samples (all brain regions) for each of the phenotyping markers (top) and pathologic markers (bottom) across all identified subpopulations. Note that pathologic markers were not used for clustering. The mean expression values were scaled across subpopulations for differential visualization purposes; note that the color bar encompasses scaled values in all subpopulations. (**B**) t-SNE plot of the AE's hidden representations of presynaptic events randomly selected from Control samples across all brain regions colored by cluster association. (**C**) Same t-SNE plot layout with each hidden representation colored by minmax-normalized expression values of markers indicative of being presynaptic particles, inhibitory neuron, and excitatory neuron. The circles highlight subpopulations that exhibit very high values of inhibitory or excitatory markers. (**D**) Subpopulation's mean frequency (±SEM) from Control samples in BA9, caudate nucleus, and hippocampus with symbols indicating Wilcoxon's $P < 0.01$ after Tukey's correction. (**E**) High correlations almost exactly at the identity line of the subpopulation frequencies between Control, ADNC, and LBD groups suggested that there were rarely any significant differences in subpopulation frequencies among the groups. Each dot represents a subpopulation frequency in a brain region. The gray lines are fitted linear lines (Spearman's R and P values) with confidence intervals, and the black lines are diagonal lines.

presynaptic molecular composition among the three groups: Control, ADNC, and LBD. Specifically, mean expression for the full complement of presynaptic markers was calculated for each subpopulation, resulting in 1530 expression features per participant (3 brain regions × 15 subpopulations × 34 antibodies; note that 4 of the starting 38 were excluded because they were used for gating). Distinct from the earlier pseudo-bulk analyses, features with complete separation between the two groups, which would result in perfect classification (table S3), were intentionally omitted in ML models to allow identification of other less strong features. From the six ML algorithms we chose for comparison (see details in Materials and Methods), an elastic net (EN) model outperformed others, achieving an area under the receiver operating curve (AUC) of 0.96 with significantly different EN predicted values for Control versus ADNC ($P = 1.6 \times 10^{-3}$; Fig. 3A); this was despite the exclusion of features with complete separation between groups, which were hippocampus PHF-tau from most subpopulations and hippocampus CD47 from six subpopulations (fig. S6). Notably, the Control sample with the highest EN predicted probability value (0.37) was the only Control individual who had been diagnosed previously as mild cognitive impairment, but at final consensus was classified as cognitively normal. False discovery rate (FDR)–adjusted P values (Q values) of each feature alongside EN's weights (Fig. 3B) confirmed pseudo-bulk analysis by showing that increased hippocampus PHF-tau mean intensity and reduced BA9 DJ1 mean intensity significantly separated ADNC from Control (Fig. 3C); both of these signals were significant in every subpopulation (Fig. 3D). An additional strong feature was increased hippocampus CD47 mean expression in ADNC (Fig. 3C), particularly in $CD47^{high}$ subpopulations (Fig. 3E), which also tended to express higher PHF-tau (Spearman's $R = 0.62$, $P < 2.2 \times 10^{-16}$). Unlike CD47 (Fig. 3E), there was no strong signal from SNAP25 (Fig. 3F and fig. S7), the other presynaptic marker. The two presynaptic markers were highly correlated ($R = 0.91$) in Controls, and remained so in the ADNC group albeit with reduced

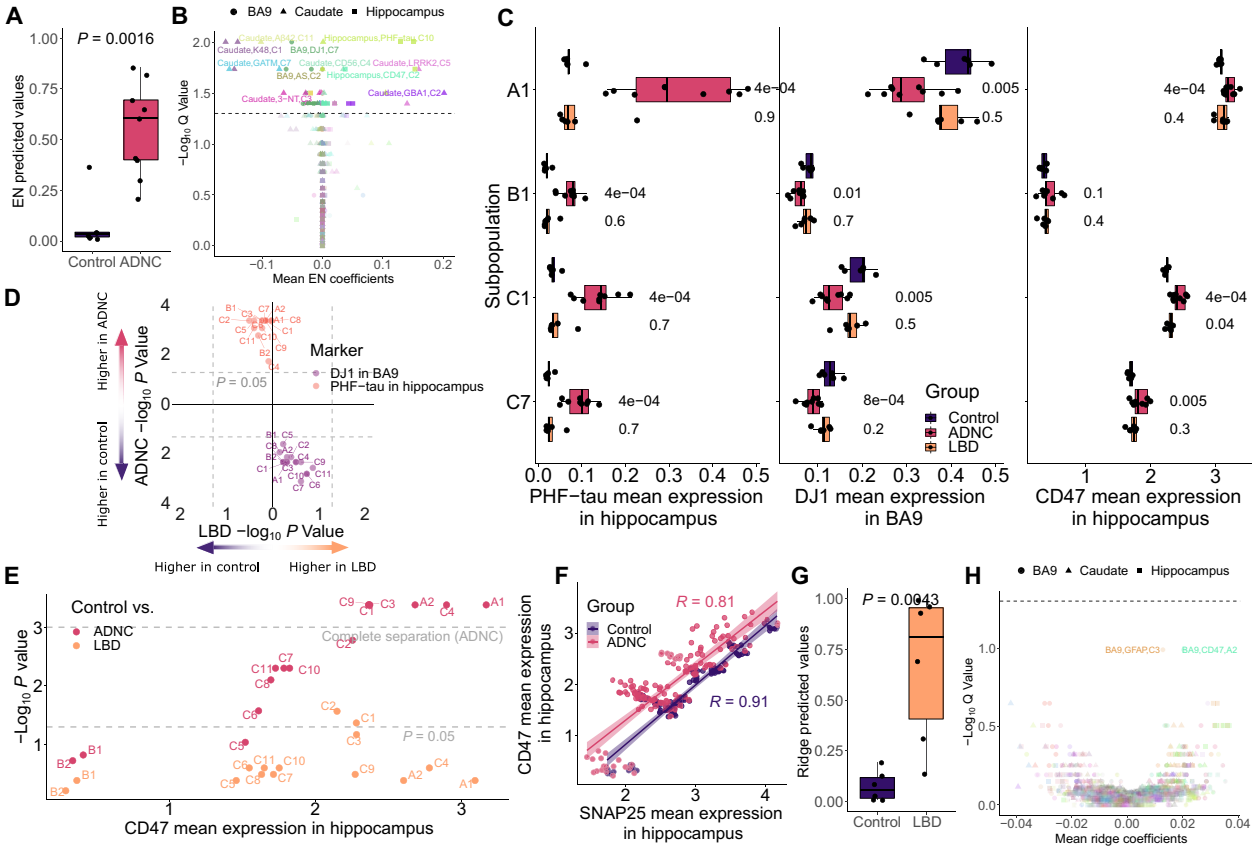

Fig. 3. Model and univariate analyses of the subpopulations identified signals unique to ADNC. (**A**) Predicted values from the EN model on Control versus ADNC. In the model, features with complete Control versus ADNC separation, such as most hippocampal PHF-tau and CD47 signals, were intentionally removed (table S3). (**B**) Visualization of important features through model's coefficients and univariate Spearman's *Q* values. The dashed line represents $Q = 0.05$. The color is unique to each expression marker, and the shape indicates brain region. (**C**) Boxplots of selected marker examples whose signal intensity was significantly different across multiple subpopulations for Control versus ADNC, including PHF-tau, DJ1, and CD47 signals. Note that CD47 signal difference in the hippocampal subpopulation B2 was not significant (Wilcoxon's *P* values) but was selected as a counterexample to support that CD47 differences were found in $CD47^{high}$ subpopulations only. (**D**) Scatterplot of $-\log_{10}$ *P* values (Wilcoxon's) of BA9's DJ1 and hippocampus's PHF-tau to highlight the significant difference of signals from these markers in all subpopulations uniquely for Control versus ADNC. (**E**) Scatterplot demonstrates that hippocampal CD47 became more significant uniquely for Control versus ADNC as its expression values increased. The mean CD47 was calculated from the mean of all samples in each disease comparison. (**F**) Scatterplot of correlations between the two presynaptic markers to highlight that they both remain highly correlated in both the ADNC and Control cases (Spearman's *R*). Each dot represents one subpopulation of a diagnosis group. (**G** and **H**) Similar to (A) and (B) for Control versus LBD samples.

correlation ($R = 0.81$) (Fig. 3F). Other expression markers exhibiting strong univariate associations with ADNC ($Q < 0.05$) or associated with high EN coefficients, but less prevalent across subpopulations, such as GATM and K48 in caudate and 3-NT in BA9, are summarized in fig. S7.

A ridge regression model outperformed other ML approaches for Control versus LBD, achieving an AUC of 0.97 and ridge predicted values ($P = 4.3 \times 10^{-3}$; Fig. 3G), even with exclusion of features with complete separation, which were lower caudate DAT from most subpopulations and higher BA9 glial fibrillary acidic protein (GFAP) from subpopulations A1 and C4 in the LBD group (table S3). In both of these subpopulations, significantly increased signals from the other astrocytic marker, EAAT1, were also observed, albeit weaker. Severe astrogliosis, even with spongiform change, in cerebral cortical superficial layers is a well-described feature of LBD but not AD (*18*, *31*). Similar to ADNC, features associated with greater ridge coefficients were those with higher univariate impact (Fig. 3H); unlike ADNC, none of the features passed the 0.05 *Q* value threshold, except for the excluded features that completely separated the two groups (table S3). This may be due, in part, to a lower number of LBD only samples, or perhaps less severe degeneration in LBD compared to ADNC (*32*). Notably, none of the top features for Control versus LBD, i.e., caudate DAT in multiple subpopulations, BA9 GFAP in C3, and BA9 CD47 in A2, overlapped with those from Control versus AD, again indicating that SynTOF identified disease-specific presynaptic molecular features.

Presynaptic features suggest molecular differences between AD dementia and AD resilient cases

Resilience describes maintained cognitive function despite high levels of pathologic change. There were two AD resilient cases among the nine ADNC analyzed, and also the only ones out of the entire original set of 113 samples (table S1). To examine their impact, these two AD resilient cases were sequestered and *Q* values were recalculated.

The analysis (six Control versus seven AD dementia) resulted in robust increase in existing signal strength and prevalence, particularly for DJ1 from more subpopulations in BA9 (Fig. 4A and fig. S7), except for PHF-tau and CD47, which remained the same. Several new signals also emerged, with the strongest being ApoE from subpopulations A1 and C5 in hippocampus (Fig. 4B). Further gating to obtain GFAP^{neg}EAAT1^{neg} presynaptic events, i.e., presynaptic events without attached astrocytic remnants, removed 11.4 ± 3.1% of presynaptic events. Analyses of the GFAP^{neg}EAAT1^{neg} presynaptic event data suggested that the ApoE signal derived from neuronal elements with and without attached astrocytic remnants (Fig. 4C). No new signal was revealed when a similar approach was used with LBD-resistant cases (not shown).

To support that these new signals obtained upon removal of two AD resilient cases were likely not coincidental, an additional analysis was conducted wherein the two AD resilient cases were retained and instead two AD dementia cases were removed and *Q* values were calculated. No significant change in antibody signal, including ApoE, occurred with sequestration of any other pair of AD dementia cases (Fig. 4A). Although limited by a small number of rare cases, our analyses suggested that the amount of hippocampal ApoE in the presynapse, tentatively in both the neuronal component and intimately associated astrocytic component, may be important to the clinical expression of dementia in AD.

MIBI-TOF analysis of tissue sections supports SynTOF findings

MIBI by TOF (MIBI-TOF) (*33*) was used to support the physical existence of AE-identified subpopulations. Akin to SynTOF, elemental isotopic reporters of *n*-dimension are used for quantitative profiling, but MIBI-TOF also determines nanometer spatial resolution. A 2.4-mm^2 region of interest (ROI) composed of six 400-μm^2 fields

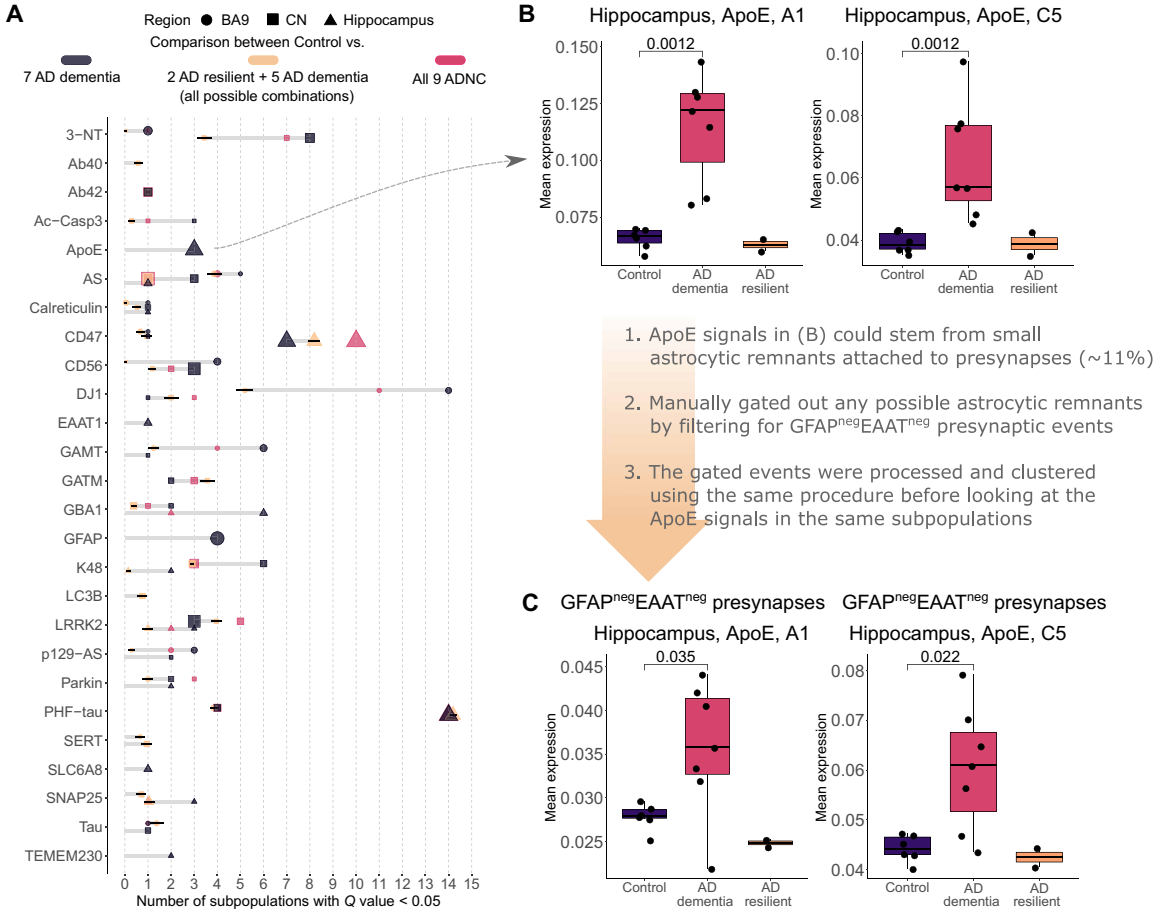

Fig. 4. Changes in significant features and signal strength within AD dementia cases. (**A**) Number of significant subpopulations after FDR adjustment (*Q* < 0.05) for each of the expression markers in different brain regions. The dark gray color indicates comparison between seven AD dementia cases and all Control cases. Tan is between all combinations (*n* = 36) of all Control cases and seven ADNC cases, i.e., five of seven AD dementia plus the two AD resilient, and therefore presented with SDs. For reference, the red color indicates the original comparison between all nine ADNC cases and the Control. The larger dot size indicates lower *Q* value. Only markers with significant subpopulations are shown. (**B**) Boxplots of the strongest, newly emerged signals for Control versus AD dementia only cases: ApoE expression from two subpopulations in the hippocampus. (**C**) Investigation into ApoE signals similar to (B) but looking strictly at presynaptic events with no astrocytic remnants. Data in (A) and (B) include the approximately 11% of events that contained attached astrocytic remnants. To assess the extent to which ApoE expression derived from neuronal events only versus the subset of presynaptic events with astrocytic remnants, we repeated our analysis with the GFAP^{neg}EAAT^{neg} filters incorporated into the previously used presynaptic gating strategy, followed by the same clustering, processing, and analyses. The results showed reduced effect size compared to all presynaptic events (B) but still remained significant, suggesting that the ApoE signal derived from both neuronal presynapse and astrocytic remnant components of the single-event data.

of view (FOVs; 1024 × 1024 pixels each) from the CA1 sector of Control and ADNC hippocampus was scanned at 300-nm resolution (Fig. 5A). Figure 5B shows example FOVs at different scales colored for synaptophysin, CD47, and PHF-tau, where the zoomed-in images suggest close proximity of some PHF-tau and CD47 pixels. Validation of SynTOF data, derived from physically enriched presynaptic particles, by MIBI-TOF requires in silico enrichment of presynapse signals versus all other signals in the tissue section; this was achieved by colocating at least two presynaptic markers. First, each pixel was agnostically assigned as positive or negative for each marker through self-organizing map clustering (Fig. 5B, see details in Materials and Methods); MIBI-TOF marker positivity is equivalent to high or very high expression in SynTOF. Second, a sliding window collected data over the entire MIBI-TOF FOV for quantitative analysis, where windows that contained $CD47^{+}Synaptophysin^{+}PSD95^{-}$ pixels were defined as presynaptic. A 6 × 6 pixel (approximately 1.8 μm^2) window was used because a presynapse is approximately 1 μm^3 in fixed and embedded tissue (*34*).

MIBI-TOF confirmed three major findings from SynTOF. First, MIBI-TOF displayed high colocalization of multiple positive markers in each sliding window, in accord with subpopulation characteristics identified by SynTOF, particularly the "high-expressers" such as subpopulation A. A heatmap and Venn diagram (Fig. 5, C and D) of a subset of SynTOF phenotypic markers used in MIBI-TOF (ApoE, CD56, GAD65, tau, and vGLUT) showed high frequency of coincident marker positivity in presynapse windows. Second, presynaptic colocation of CD47 and PHF-tau observed in SynTOF was also observed by MIBI. Figure 5E shows that about half of the $CD47^{+}$ presynaptic windows also had $PHF\text{-}tau^{+}$ pixels. This result was consistent even if the positivity cutoff for the number of pixels was increased. Last, the average level of expression of PHF-tau and CD47 was both higher in ADNC presynaptic windows than in

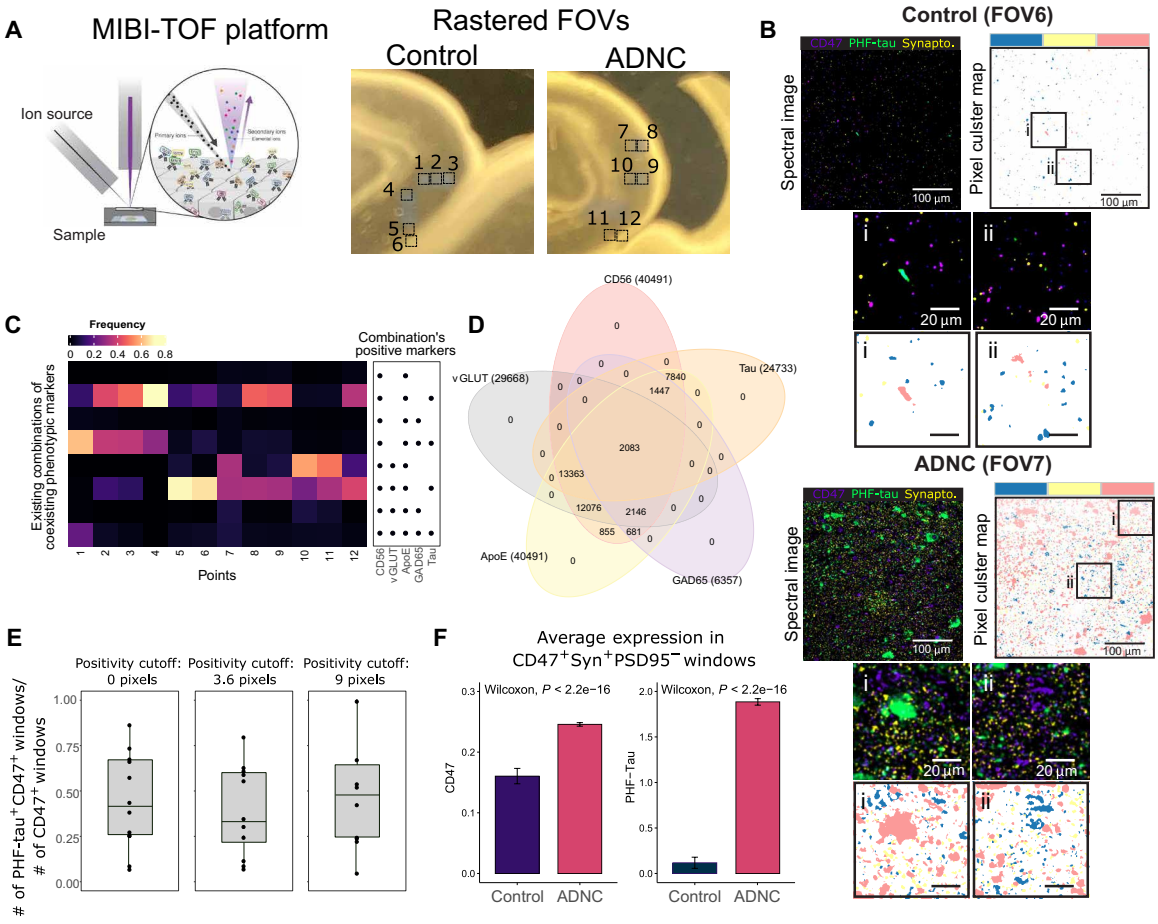

Fig. 5. Analysis of MIBI-TOF images supports SynTOF findings by suggesting high colocalization of phenotypic markers, colocalization of CD47 and PHF-tau, and higher CD47 expression in ADNC. (**A**) Illustration of MIBI-TOF and the sampled locations of the FOVs from CA1 sector of the hippocampus. (**B**) Examples of MIBI-TOF image FOV from Control and ADNC. The spectral images are overlaid with CD47, PHF-tau, and synaptophysin channels for identification of likely synapses (left) with corresponding areas colored by CD47-positive (blue), PHF-tau–positive (pink), and synaptophysin-positive (yellow) clusters obtained from self-organizing maps clustering (right). Bottom, smaller panels show zoomed-in images within the rectangles. (**C**) Heatmap showing existing combinations of positive MIBI's phenotypic markers found from aggregated sliding windows, with colors representing a fraction of positivity over the number of presynaptic windows defined as containing $CD47^{+}Synaptophysin^{+}PSD95^{-}$. (**D**) Venn diagram summarizing the intersected expression of the phenotypic markers. The number in the parenthesis indicates the total number of positive windows. (**E**) Boxplots showing the fraction of PHF-tau and CD47 colocalization within a window over different numbers of pixel cutoffs used for defining marker positivity. (**F**) Barplots showing higher average (±SEM) CD47 and PHF-tau expressions in ADNC based on all presynaptic windows in all points.

Control, again validating SynTOF results (Fig. 5F). All analyses were also repeated using 3 × 3 pixel and 9 × 9 pixel window sizes and arrived at the same conclusions (fig. S8). In aggregate, using a complementary method on intact tissue, MIBI-TOF data confirmed the major findings from SynTOF.

DISCUSSION

The anatomical basis for cognitive decline in AD and LBD is synaptic injury. SynTOF has advantages over other techniques that molecularly characterize single-synapse events from synaptosome preparations: (i) further computational enrichment of single-synapse events by error correction and sequential gating, (ii) greater than an order of magnitude increases in detection of enriched single-synapse events, and (iii) an order of magnitude increase in number of multiplex antibody probes. We built our SynTOF panel to focus on phenotypic markers, products of risk genes, and mechanisms relevant to AD or LBD. As shown previously with conventional flow cytometry (*35*) and replicated here with SynTOF, human synaptosomes maintain molecular integrity at least as compared to NHP samples collected and prepared under optimal research conditions. Results from our SynTOF panel aligned well with ultrastructural estimates of the regional proportions of synaptic subtypes and with array tomography estimates of synaptic involvement by hallmark pathologic proteins. Furthermore, MIBI-TOF colocalization of prominent molecular features supported the major outcomes of AE-identified subpopulations. Thus buttressed, SynTOF unveiled key differences in presynaptic molecular composition between late-onset AD and aged PS/APP mice, reinforced the relevance of synaptic pathologic tau species in AD (*36*), and highlighted presynaptic roles for CD47, DJ1, and ApoE in AD.

Mass spectrometry–based proteomic studies on synaptosome preparations have identified more than 3000 proteins [reviewed in (*10*)], ~1000 of which are conserved across the vertebrate species zebrafish and mice; these include the homologs of DJ1 and ApoE but not CD47, which was identified only in mouse brain synaptosomes (*37*). Although recent studies have used mass spectrometry to investigate the proteomic changes in brain samples from individuals with AD or without neurologic disease, few have examined the proteome of human synaptosomes using modern proteomic techniques (*11*, *12*). An exception is a recent preprint that described proteomic changes in synaptosomes from individuals resilient to the clinical expression of dementia in the context of high neuropathologic changes of AD (*38*). Future applications of our complementary approach with SynTOF will focus on these and other clinicopathologic subsets that likely hold key insights into the mechanisms of AD (*20*).

Mutations in *PARK7*, the gene that encodes DJ1, cause an autosomal recessive form of early-onset PD and, for this reason, were included in our SynTOF panel. DJ1 functions as a redox-sensitive chaperone and antioxidant. It is a target for reversible and irreversible oxidative modification in brains of patients not only with PD but also with late-onset AD, where it may incorporate in hallmark lesions like Lewy bodies and amyloid plaques (*39*, *40*). These pathologic changes are proposed to underlie the significant accumulation of DJ1 in the detergent-insoluble fraction of bulk tissue from affected regions of the brain in AD and LBD (*39*, *41*, *42*). Our results showed significantly reduced BA9 presynaptic DJ1, which is consistent with these findings from others, and support the hypothesis that increased oxidative stress can lead to posttranslational modifications of synaptic DJ1 that result in its shift to nonsynaptic compartments. We observed significant reduction in presynaptic DJ1 only in AD, consistent with earlier data showing that oxidative damage is greater in AD than in LBD and other related dementias (*43*).

Forced expression of CD47 in cultured hippocampal neurons accumulates at presynaptic sites and acts as the presynaptic receptor for the shed ectodomain of signal regulatory protein α (SIRPα) in activity-dependent trans-synaptic maturation of functional synapses (*44*, *45*). CD47 is also expressed on myeloid cells and has been shown to affect microglial and macrophage activity in mouse models of multiple sclerosis and cell culture models using Aβ peptides (*46*, *47*). CD47, an immune "don't eat me signal," protects from excess microglia-mediated synaptic pruning during mouse development (*48*), but as far as we are aware, there has been no investigation of synaptic CD47 in brain aging or neurodegenerative disease. Our results showed that presynaptic CD47 was significantly elevated in AD hippocampus, with less robust increases in LBD hippocampus or BA9 for both diagnostic groups; caudate presynaptic CD47 was not different among the three primary diagnostic groups. Because activated microglia-mediated neuronal injury is now a well-established mechanism in AD (*49*), we hypothesize that increased presynaptic CD47 is a response to limit or counteract synaptic degradation by microglia in hippocampus and likely cerebral cortex. Our discovery of elevated CD47 in AD hippocampus presynaptic events, which also tended to coexpress with PHF-tau, is especially encouraging because of emerging CD47-targeting therapeutics in certain forms of cancer (*50*).

There is intense interest in where resilience may reside in the cascade from synaptic injury to symptoms because this may illuminate effective therapeutic targets. Our results suggest that resilience to AD may be related to lower ApoE levels in presynaptic events, in either neuronal components or attached associated astrocytic remnants. Multiple experimental models support this proposal at the tissue level. For example, *ApoE* deletion or haploinsufficiency reduces cerebral Aβ amyloidosis and rescues from tau-induced neurodegeneration (*51*, *52*). Moreover, approximately 50% reduction of brain ApoE in a humanized transgenic mouse model of AD reduced neuronal injury perhaps from suppressed glial response from lowered ApoE levels (*53*). Although limited by a small number of rare resilient cases, our results from human presynaptic events align with multiple experimental models to suggest that lower levels of presynaptic ApoE are a significant component of the resilient state.

Our pseudo-bulk analysis showed that only a small subset of human presynaptic events had detectable Aβ peptides, similar to previous work (*13*), and that synaptic Aβ peptides were not increased in AD. We showed that synaptic particles with accumulated Aβ peptides survive synaptosome preparation and downstream analysis by investigating aged PS/APP mice for which there is a large amount of experimental data supporting increased synaptic Aβ peptides (*28*). The pattern of presynaptic injury and response in PS/APP mice was different from human AD samples. It is possible that the transgenic mice reflect a different stage of disease than humans with sporadic AD (*29*), but this is unlikely the sole explanation for the differences in presynaptic changes because the brain autopsies were from people with high-level ADNC at all stages of cognition, a rough proxy for extent of neurodegeneration. A more direct comparison to PS/APP mice would be individuals with *APP* or *PSEN1* mutations; however, as far as we are aware, no appropriately prepared tissue from individuals with these disease-causing mutations exists in the world. Together, our results support a role for Aβ peptide–mediated presynaptic injury in PS/APP mice, but caution that there is a critical

difference in the synaptic distribution of Aβ peptides between aged PS/APP mice and people with sporadic, high-level ADNC.

In summary, SynTOF provides an unparalleled opportunity for multiplex analysis of millions of single-synapse events. Results from our current panel of 34 antibodies implicated pathologic tau, immune-mediated pruning, and oxidative injury, but not increased Aβ peptide accumulation, as key components of synaptic injury in AD, and synapse-associated ApoE as important in the clinical expression of dementia.

MATERIALS AND METHODS

Study design

The research goal is to investigate synaptic molecular changes in brain samples from individuals with ADNC and LBD. All brain donations were from research volunteers at Stanford University or the University of Washington. All participants provided informed consent approved by Institutional Review Boards. Clinical and pathological diagnoses followed consensus criteria (*18*, *31*, *54*). One hundred thirteen samples were collected and cryopreserved prospectively from brain autopsies with short postmortem interval (PMI < 8 hours) over a 5-year period; only those that met stringent clinical and pathological criteria for Control ($n = 6$), ADNC ($n = 9$), and LBD ($n = 6$) were used for this study (table S1) (*16*, *35*).

Brain regional synaptosome preparations from female *Macaca fascicularis* ($n = 4$) collected under research protocols were used to assess the integrity of human synaptosomes collected through rapid autopsy. All NHP procedures were performed at Wake Forest University (Winston-Salem, NC) with approval from the Institutional Animal Care and Use Committee, according to recommendations in the *Guide for Care and Use of Laboratory Animals* (Institute for Laboratory Animal Research), and in compliance with the U.S. Department of Agriculture Animal Welfare Act and Animal Welfare Regulations (Animal Welfare Act as Amended; Animal Welfare Regulations). NHPs were sacrificed at 11.5 ± 0.3 years of age, brains were immediately removed, and regions were collected for synaptosome preparation using the same human protocol as previously described by us (*35*). NHP samples were prepared for mass cytometry, and data were acquired and processed exactly as for human samples (*17*) as described below.

PS/APP ($n = 5$) and C57Bl6 WT ($n = 5$) male mice were used for evaluating Aβ-containing synaptosome preparations and for comparison with humans. All mouse procedures were conducted in accordance with the guidelines of the Institutional Animal Care and Use Committee at Stanford University. Mice were sacrificed at 22 months of age, their brains were rapidly removed, and brain regions were collected for synaptosome preparation as previously described (*16*, *35*).

SynTOF antibodies and sample preparation

Overall, we conjugated and screened 166 antibodies and brought forward those 38 that had highest specificity and sensitivity for each target (for example, we selected pan-vGLUT to capture all isoforms). The limit of detection for the Helios mass cytometer used is <0.1 parts per trillion (*55*). Across the SynTOF panel, signal:noise ranged from 10 to 371 (average 96) and coefficient of variation ($n = 4$ replicates) averaged 8.2 ± 4.5%. Antibody specificity was assessed using established criteria (table S4) (*56*). Among the 38 antibodies in the panel, four were used for manual gating to exclude nonpresynaptic events (CD11b, gephyrin, PSD95, and MBP) and were removed from downstream analyses. The remaining 34 expression markers (Figs. 1A and 2A) were selected to investigate five features: neuron type, product of genetic risk factor for AD, product of genetic risk factor for LBD, injury/response, and cellular energy (Fig. 1A). The 34 expression markers were further subdivided into 24 phenotypic markers (table S2) to facilitate clustering of presynaptic events (Fig. 2A) and 10 pathologic markers (table S2: Aβ40, Aβ42, PHF-tau, p-129-α-synuclein, Ac-Casp3, 3-NT, EAAT1, K48, LC3B, and GFAP).

Following our established protocol (*17*), samples were processed and mass synaptometry data were acquired, barcoded/debarcoded, and gated for % positive events exactly as described by us (*14*) with the exception of adding gephyrin to PSD95 to gate for postsynaptic events. No samples were regarded as outliers or excluded. Human synaptosome preparations were analyzed to detect approximately 100 million events. Debarcoding and sequential gating (*17*) yielded highly enriched single-presynaptic ($n = 14{,}904{,}100$) and single-postsynaptic ($n = 823{,}280$) events from BA9 of human prefrontal cortex, caudate nucleus, and hippocampus (synaptosome preparations strongly favor pre- over postsynaptic particles). Using the same method and multiplex panel, we also assayed >740,000 single-presynaptic events from NHP frontal cortex and striatum, and >440,000 single-presynaptic events from cerebral cortex and hippocampus of 22-month-old WT C57Bl6 and PS/APP transgenic mice (*57*).

Clustering of single-synapse events

Cellular population assignment through clustering algorithms has developed rapidly in recent years (*58*–*61*). In our model, an AE was used to cluster single-synapse events to different subpopulations. AE is a type of neural network typically with a bottleneck layer that generates compressed representations of the single-synapse data by learning to reconstruct them. Our model is adapted from a variant of AE called Improved Deep Embedded Clustering (IDEC) (*62*), which adds to typical AE a clustering network layer that clusters single-synapse data based on the obtained compressed representation. This method was selected over traditional single-event clustering algorithms, such as FlowSOM, SPADE, or *k*-means, due to its higher cluster assignment accuracy compared to benchmarked manual gating on publicly available datasets.

In our model, two identical AEs with different numbers of bottleneck nodes were used. The node sizes for each layer were [512, 256, 128, 10, 128, 256, 512] and [512, 256, 128, 5, 128, 256, 512]. The AEs were separately pretrained to reconstruct the single-presynaptic events from all brain regions of all six Control samples using mean square error (MSE) for loss function and adaptive gradient method for optimization (Adagrad). After pretraining, a clustering layer was appended to the AEs, where its input was a concatenated hidden representation from the two bottleneck layers. The weights of the clustering layer were initiated using centers from *k*-means clustering. Its number of nodes, which dictated the number of clusters, was determined using an elbow method, i.e., the number of clusters at which the within-cluster sum of squared errors (WSS) plateaus. This new architecture was then trained to minimize the following WSS plateaus. This new architecture was then trained to minimize the following loss function

$$L = \sum_{n}^{2} L_r + \gamma \sum_{i} \sum_{j} p_{ij} \log \frac{p_{ij}}{q_{ij}}$$

where the first term is the summation of MSE loss for reconstruction of the two AEs and the second term is the clustering assignment

hardening loss with proportion modulated by γ of 1. The clustering loss was calculated by

$$q_{ij} = \frac{(1 + \|z_i - \mu_j\|^2)^{-1}}{\Sigma_j (1 + \|z_i - \mu_j\|^2)^{-1}}$$

$$p_{ij} = \frac{q_{ij}^2 / \Sigma_i q_{ij}}{\Sigma_j (q_{ij}^2 / \Sigma_i q_{ij})}$$

where q_{ij} is the normalized similarity between hidden representation point z_i to cluster centroid μ_j by Student's t-distribution measure and can be considered as soft cluster assignments, while p_{ij} served as stricter (hardened) auxiliary ground truth labels on which the model trained. Therefore, p_{ij} was not updated after every batch interval, but every 700 to allow convergent cluster layer training. The entire AE model was trained until the hard cluster assignment calculated by argmax(q_{ij}) became less than 5% difference compared to the last update. To leverage inherent randomness within neural networks, these steps were repeated 10 times and the final cluster assignment was obtained from meta-clustering (greedy algorithm by Dimitriadou, Weingessel, and Hornik) of the hard cluster assignment obtained from each of the iterations (*63*). The trained model was then used to predict cluster assignment for postsynaptic events and presynaptic events of other diagnostic groups.

For each cluster and brain region in a given sample, a mean value for each of the 34 expression markers was calculated, yielding a total of 1530 expression features per participant (3 brain regions × 34 markers × 15 subpopulations). Mean expression values were used instead of median because some phenotypic marker's expression was rare. In addition, to improve signal quality, for expression markers AS, CD47, DAT, GAD65, Synaptobrevin2, vGLUT, and VMAT2 in subpopulations B1 and B2, which overlapped with postsynaptic events (fig. S5, D to F), their values were subtracted by mean values from the corresponding postsynaptic subpopulations, as these markers were known to be highly enriched in presynapses. The preliminary robustness and sanity check of the resulting clusters compared to existing literature (*64*, *65*) are detailed in the Supplementary Materials.

ML model evaluation and interpretation

Similar to single-cell analyses in AD and other diseases (*66*, *67*), conventional ML models were used for prediction and identification of important features. The input to the models was the mean expression matrix obtained after clustering. For all of the classification and regression tasks in this study, five ML algorithms were compared, including LASSO, ridge, EN, random forest, extreme gradient boosting (XGBoost), and support vector machine (SVM). Only the best performing model was reported. All of the models were run on Python using either sklearn or xgboost packages with default hyperparameters, as optimizing these models to obtain the best possible prediction results was not the goal of this study. A leave-one-out cross-validation method was used to evaluate the performance of each of the models. The aggregated test prediction values were used for evaluation. The AUC and Wilcoxon's P value were used as criteria.

MIBI for identification of subpopulation characteristics suggested by SynTOF

ADNC and Control hippocampus samples from different brain autopsies than those used for SynTOF were sectioned at 4-mm thickness from archival formalin fixed paraffin embedded tissue blocks and mounted on salinized gold slides for MIBI-TOF. MIBI-TOF antibody conjugation and staining exactly followed previously published protocols (*68*, *69*). Acquisition of spectral images was performed using a modified MIBI-TOF (Oregon Physics & IONPATH) with a hyperion ion source (*33*). Images were preprocessed as described previously (*33*).

To assign meaningful phenotypes to each pixel of the image, we applied a pixel clustering approach. Preprocessed (background-subtracted, denoised) MIBI images were first Gaussian blurred using an SD of 2 for the Gaussian kernel. Pixels were normalized by their total expression such that the total expression of each pixel was equal to 1. A 99.9% normalization was applied for each marker. Pixels were clustered into 100 clusters using FlowSOM based on the expression of the markers. The average expression of each of the 100 pixel clusters was found, and the z score for each marker across the 100 pixel clusters was computed. All z scores were capped at 3 such that the maximum z score was 3. Using these z-scored expression values, the 100 pixel clusters were clustered using consensus hierarchical clustering using Euclidean distance into 20 metaclusters. In our experience, for a set of 16 clustering markers, 20 metaclusters are able to capture the phenotypic diversity well. Upon inspection of the expression heatmap of the 20 metaclusters, we observed discrete phenotypes for each metacluster. These metaclusters were mapped back to the original images to generate overlay images colored by pixel metacluster. Each pixel was therefore assigned to an interpretable phenotypic cluster.

We then applied a sliding window approach to assess the colocalization of proteins within each image. We varied the size of the sliding window, using 3 × 3 pixel windows (0.9 μm^2) with a stride of 2 pixels, 6 × 6 pixel windows (0.9 μm^2) with a stride of 3 pixels, and 9 × 9 pixel windows (2.7 μm^2) with a stride of 3 pixels. Results were consistent across different window sizes. For each window, we assessed marker positivity by counting the number of pixels of each pixel cluster within each window. For example, if a window contained a pixel belonging to pixel cluster 1, which was defined by the tau expression, the window was called as tau$^+$. For each window, we assessed marker positivity for CD56, vGLUT, ApoE, GAD65, and tau. We varied the cutoff for calling positivity, and results were consistent across different cutoffs. By using such an approach, we identified which markers were expressed in each window. By assessing combinations of markers within each window, we could investigate marker colocalization.

Furthermore, we assessed the mean expression of CD47 and PHF-tau within each window. The MIBI images were transformed by multiplying by 100 and arcsinh-transformed with a cofactor of 5 and then rescaled on a 0 to 5 scale. The images were then normalized by average histone H3 (HH3) expression to mitigate batch effects between MIBI images, because average HH3 expression is consistent across images (*33*). The average expression of CD47 and PHF-tau was then calculated using these normalized values.

SUPPLEMENTARY MATERIALS

Supplementary material for this article is available at https://science.org/doi/10.1126/sciadv.abk0473

View/request a protocol for this paper from *Bio-protocol*.

REFERENCES AND NOTES

1. S. W. Scheff, D. A. Price, Synaptic pathology in Alzheimer's disease: A review of ultrastructural studies. *Neurobiol. Aging* **24**, 1029–1046 (2003).

2. R. D. Terry, E. Masliah, D. P. Salmon, N. Butters, R. DeTeresa, R. Hill, L. A. Hansen, R. Katzman, Physical basis of cognitive alterations in Alzheimer's disease: Synapse loss is the major correlate of cognitive impairment. *Ann. Neurol.* **30**, 572–580 (1991).
3. E. Masliah, R. D. Terry, M. Alford, R. DeTeresa, L. A. Hansen, Cortical and subcortical patterns of synaptophysinlike immunoreactivity in Alzheimer's disease. *Am. J. Pathol.* **138**, 235–246 (1991).
4. B. T. Hyman, G. W. Van Hoesen, L. J. Kromer, A. R. Damasio, Perforant pathway changes and the memory impairment of Alzheimer's disease. *Ann. Neurol.* **20**, 472–481 (1986).
5. S. T. DeKosky, S. W. Scheff, Synapse loss in frontal cortex biopsies in Alzheimer's disease: Correlation with cognitive severity. *Ann. Neurol.* **27**, 457–464 (1990).
6. K. H. Gylys, T. Bilousova, Flow cytometry analysis and quantitative characterization of tau in synaptosomes from Alzheimer's disease brains. *Methods Mol. Biol.* **1523**, 273–284 (2017).
7. B. C. Yoo, N. Cairns, M. Fountoulakis, G. Lubec, Synaptosomal proteins, beta-soluble N-ethylmaleimide-sensitive factor attachment protein (beta-SNAP), gamma-SNAP and synaptotagmin I in brain of patients with Down syndrome and Alzheimer's disease. *Dement. Geriatr. Cogn. Disord.* **12**, 219–225 (2001).
8. T. S. Wijasa, M. Sylvester, N. Brocke-Ahmadinejad, S. Schwartz, F. Santarelli, V. Gieselmann, T. Klockgether, F. Brosseron, M. T. Heneka, Quantitative proteomics of synaptosome S-nitrosylation in Alzheimer's disease. *J. Neurochem.* **152**, 710–726 (2020).
9. B. G. Perez-Nievas, T. D. Stein, H. C. Tai, O. Dols-Icardo, T. C. Scotton, I. Barroeta-Espar, L. Fernandez-Carballo, E. L. de Munain, J. Perez, M. Marquie, A. Serrano-Pozo, M. P. Frosch, V. Lowe, J. E. Parisi, R. C. Petersen, M. D. Ikonomovic, O. L. López, W. Klunk, B. T. Hyman, T. Gómez-Isla, Dissecting phenotypic traits linked to human resilience to Alzheimer's pathology. *Brain* **136**, 2510–2526 (2013).
10. F. Koopmans, P. van Nierop, M. Andres-Alonso, A. Byrnes, T. Cijsouw, M. P. Coba, L. N. Cornelisse, R. J. Farrell, H. L. Goldschmidt, D. P. Howrigan, N. K. Hussain, C. Imig, A. P. H. de Jong, H. Jung, M. Kohansalnodehi, B. Kramarz, N. Lipstein, R. C. Lovering, H. M. Gillavry, V. Mariano, H. Mi, M. Ninov, D. Osumi-Sutherland, R. Pielot, K.-H. Smalla, H. Tang, K. Tashman, R. F. G. Toonen, C. Verpelli, R. Reig-Viader, K. Watanabe, J. van Weering, T. Achsel, G. Ashrafi, N. Asi, T. C. Brown, P. De Camilli, M. Feuermann, R. E. Foulger, P. Gaudet, A. Joglekar, A. Kanellopoulos, R. Malenka, R. A. Nicoll, C. Pulido, J. de Juan-Sanz, M. Sheng, T. C. Südhof, H. U. Tilgner, C. Bagni, À. Bayés, T. Biederer, N. Brose, J. J. E. Chua, D. C. Dieterich, E. D. Gundelfinger, C. Hoogenraad, R. L. Huganir, R. Jahn, P. S. Kaeser, E. Kim, M. R. Kreutz, P. S. McPherson, B. M. Neale, V. O'Conner, D. Posthuma, T. A. Ryan, C. Sala, G. Feng, S. E. Hyman, P. D. Thomas, A. B. Smit, M. Verhage, SynGO: An evidence-based, expert-curated knowledge base for the synapse. *Neuron* **103**, 217–234.e4 (2019).
11. E. C. B. Johnson, E. B. Dammer, D. M. Duong, L. Ping, M. Zhou, L. Yin, L. A. Higginbotham, A. Guajardo, B. White, J. C. Troncoso, M. Thambisetty, T. J. Montine, E. B. Lee, J. Q. Trojanowski, T. G. Beach, E. M. Reiman, V. Haroutunian, M. Wang, E. Schadt, B. Zhang, D. W. Dickson, N. Ertekin-Taner, T. E. Golde, V. A. Petyuk, P. L. de Jager, D. A. Bennett, T. S. Wingo, S. Rangaraju, I. Hajjar, J. M. Shulman, J. J. Lah, A. I. Levey, N. T. Seyfried, Large-scale proteomic analysis of Alzheimer's disease brain and cerebrospinal fluid reveals early changes in energy metabolism associated with microglia and astrocyte activation. *Nat. Med.* **26**, 769–780 (2020).
12. A. P. Wingo, E. B. Dammer, M. S. Breen, B. A. Logsdon, D. M. Duong, J. C. Troncosco, M. Thambisetty, T. G. Beach, G. E. Serrano, E. M. Reiman, R. J. Caselli, J. J. Lah, N. T. Seyfried, A. I. Levey, T. S. Wingo, Large-scale proteomic analysis of human brain identifies proteins associated with cognitive trajectory in advanced age. *Nat. Commun.* **10**, 1619 (2019).
13. C. M. Henstridge, R. J. Jackson, J. S. M. Kim, A. G. Herrmann, A. K. Wright, S. E. Harris, M. E. Bastin, J. M. Starr, J. Wardlaw, T. H. Gillingwater, C. Smith, C. A. McKenzie, S. R. Cox, I. J. Deary, T. L. Spires-Jones, Post-mortem brain analyses of the Lothian Birth Cohort 1936: Extending lifetime cognitive and brain phenotyping to the level of the synapse. *Acta Neuropathol. Commun.* **3**, 53 (2015).
14. M. Colom-Cadena, J. Pegueroles, A. G. Herrmann, C. M. Henstridge, L. Muñoz, M. Querol-Vilaseca, C. S. Martín-Paniello, J. Luque-Cabecerans, J. Clarimon, O. Belbin, R. Núñez-Llaves, R. Blesa, C. Smith, C. A. McKenzie, M. P. Frosch, A. Roe, J. Fortea, J. Andilla, P. Loza-Alvarez, E. Gelpi, B. T. Hyman, T. L. Spires-Jones, A. Lleó, Synaptic phosphorylated α-synuclein in dementia with Lewy bodies. *Brain* **140**, 3204–3214 (2017).
15. H. C. Tai, B. Y. Wang, A. Serrano¿Pozo, M. P. Frosch, T. L. Spires-Jones, B. T. Hyman, Frequent and symmetric deposition of misfolded tau oligomers within presynaptic and postsynaptic terminals in Alzheimer¿s disease. *Acta Neuropathol. Commun.* **2**, 146 (2014).
16. C. R. Gajera, R. Fernandez, N. Postupna, K. S. Montine, E. J. Fox, D. Tebaykin, M. Angelo, S. C. Bendall, C. D. Keene, T. J. Montine, Mass synaptometry: High-dimensional multi parametric assay for single synapses. *J. Neurosci. Methods* **312**, 73–83 (2019).
17. C. R. Gajera, R. Fernandez, K. S. Montine, E. J. Fox, D. Mrdjen, N. O. Postupna, C. D. Keene, S. C. Bendall, T. J. Montine, Mass-tag barcoding for multiplexed analysis of human synaptosomes and other anuclear events. *Cytometry A* **99**, 939–945 (2021).
18. B. T. Hyman, C. H. Phelps, T. G. Beach, E. H. Bigio, N. J. Cairns, M. C. Carrillo, D. W. Dickson, C. Duyckaerts, M. P. Frosch, E. Masliah, S. S. Mirra, P. T. Nelson, J. A. Schneider, D. R. Thal, B. Thies, J. Q. Trojanowski, H. V. Vinters, T. J. Montine, National Institute on Aging-Alzheimer's Association guidelines for the neuropathologic assessment of Alzheimer's disease. *Alzheimers Dement.* **8**, 1–13 (2012).
19. T. J. Montine, C. H. Phelps, T. G. Beach, E. H. Bigio, N. J. Cairns, D. W. Dickson, C. Duyckaerts, M. P. Frosch, E. Masliah, S. S. Mirra, P. T. Nelson, J. A. Schneider, D. R. Thal, J. Q. Trojanowski, H. V. Vinters, B. T. Hyman; National Institute on Aging; Alzheimer's Association, National Institute on Aging-Alzheimer's Association guidelines for the neuropathologic assessment of Alzheimer's disease: A practical approach. *Acta Neuropathol.* **123**, 1–11 (2012).
20. T. J. Montine, S. A. Bukhari, L. R. White, Cognitive impairment in older adults and therapeutic strategies. *Pharmacol. Rev.* **73**, 152–162 (2021).
21. P. Somogyi, G. Tamás, R. Lujan, E. H. Buhl, Salient features of synaptic organisation in the cerebral cortex. *Brain Res. Brain Res. Rev.* **26**, 113–135 (1998).
22. J. P. Bolam, E. K. Pissadaki, Living on the edge with too many mouths to feed: Why dopamine neurons die. *Mov. Disord.* **27**, 1478–1483 (2012).
23. J. F. Smiley, P. S. Goldman-Rakic, Heterogeneous targets of dopamine synapses in monkey prefrontal cortex demonstrated by serial section electron microscopy: A laminar analysis using the silver-enhanced diaminobenzidine sulfide (SEDS) immunolabeling technique. *Cereb. Cortex* **3**, 223–238 (1993).
24. C. J. Lacey, J. Boyes, O. Gerlach, L. Chen, P. J. Magill, J. P. Bolam, GABA(B) receptors at glutamatergic synapses in the rat striatum. *Neuroscience* **136**, 1083–1095 (2005).
25. V. J. Roberts, S. L. Barth, H. Meunier, W. Vale, Hybridization histochemical and immunohistochemical localization of inhibin/activin subunits and messenger ribonucleic acids in the rat brain. *J. Comp. Neurol.* **364**, 473–493 (1996).
26. G. W. Miller, J. D. Erickson, J. T. Perez, S. N. Penland, D. C. Mash, D. B. Rye, A. I. Levey, Immunochemical analysis of vesicular monoamine transporter (VMAT2) protein in Parkinson's disease. *Exp. Neurol.* **156**, 138–148 (1999).
27. J. Booij, G. Tissingh, G. J. Boer, J. D. Speelman, J. C. Stoof, A. G. Janssen, E. C. Wolters, E. A. van Royen, [123I]FP-CIT SPECT shows a pronounced decline of striatal dopamine transporter labelling in early and advanced Parkinson's disease. *J. Neurol. Neurosurg. Psychiatry* **62**, 133–140 (1997).
28. H. Sasaguri, P. Nilsson, S. Hashimoto, K. Nagata, T. Saito, B. de Strooper, J. Hardy, R. Vassar, B. Winblad, T. C. Saido, APP mouse models for Alzheimer's disease preclinical studies. *EMBO J.* **36**, 2473–2487 (2017).
29. L. Mucke, D. J. Selkoe, Neurotoxicity of amyloid β-protein: Synaptic and network dysfunction. *Cold Spring Harb. Perspect. Med.* **2**, a006338 (2012).
30. N. Aghaeepour, E. F. Simonds, D. J. H. F. Knapp, R. V. Bruggner, K. Sachs, A. Culos, P. F. Gherardini, N. Samusik, G. K. Fragiadakis, S. C. Bendall, B. Gaudilliere, M. S. Angst, C. J. Eaves, W. A. Weiss, W. J. Fantl, G. P. Nolan, GateFinder: Projection-based gating strategy optimization for flow and mass cytometry. *Bioinformatics* **34**, 4131–4133 (2018).
31. I. G. McKeith, B. F. Boeve, D. W. Dickson, G. Halliday, J. P. Taylor, D. Weintraub, D. Aarsland, J. Galvin, J. Attems, C. G. Ballard, A. Bayston, T. G. Beach, F. Blanc, N. Bohnen, L. Bonanni, J. Bras, P. Brundin, D. Burn, A. Chen-Plotkin, J. E. Duda, O. el-Agnaf, H. Feldman, T. J. Ferman, D. ffytche, H. Fujishiro, D. Galasko, J. G. Goldman, S. N. Gomperts, N. R. Graff-Radford, L. S. Honig, A. Iranzo, K. Kantarci, D. Kaufer, W. Kukull, V. M. Y. Lee, J. B. Leverenz, S. Lewis, C. Lippa, A. Lunde, M. Masellis, E. Masliah, P. McLean, B. Mollenhauer, T. J. Montine, E. Moreno, E. Mori, M. Murray, J. T. O'Brien, S. Orimo, R. B. Postuma, S. Ramaswamy, O. A. Ross, D. P. Salmon, A. Singleton, A. Taylor, A. Thomas, P. Tiraboschi, J. B. Toledo, J. Q. Trojanowski, D. Tsuang, Z. Walker, M. Yamada, K. Kosaka, Diagnosis and management of dementia with Lewy bodies: Fourth consensus report of the DLB Consortium. *Neurology* **89**, 88–100 (2017).
32. M. Ballmaier, J. T. O'Brien, E. J. Burton, P. M. Thompson, D. E. Rex, K. L. Narr, I. G. McKeith, H. DeLuca, A. W. Toga, Comparing gray matter loss profiles between dementia with Lewy bodies and Alzheimer's disease using cortical pattern matching: Diagnosis and gender effects. *NeuroImage* **23**, 325–335 (2004).
33. L. Keren, M. Bosse, S. Thompson, T. Risom, K. Vijayaragavan, E. M. Caffrey, D. Marquez, R. Angoshtari, N. F. Greenwald, H. Fienberg, J. Wang, N. Kambham, D. Kirkwood, G. Nolan, T. J. Montine, S. J. Galli, R. West, S. C. Bendall, M. Angelo, MIBI-TOF: A multiplexed imaging platform relates cellular phenotypes and tissue structure. *Sci. Adv.* **5**, eaax5851 (2019).
34. V. Rangaraju, N. Calloway, T. A. Ryan, Activity-driven local ATP synthesis is required for synaptic function. *Cell* **156**, 825–835 (2014).
35. N. Postupna, C. S. Latimer, E. B. Larson, E. Sherfield, J. Paladin, C. A. Shively, M. J. Jorgensen, R. N. Andrews, J. R. Kaplan, P. K. Crane, K. S. Montine, S. Craft, C. D. Keene, T. J. Montine, Human striatal dopaminergic and regional serotonergic synaptic degeneration with lewy body disease and inheritance of APOE ε4. *Am. J. Pathol.* **187**, 884–895 (2017).
36. M. Gratuze, D. M. Holtzman, Targeting pre-synaptic tau accumulation: A new strategy to counteract tau-mediated synaptic loss and memory deficits. *Neuron* **109**, 741–743 (2021).

37. À. Bayés, M. O. Collins, R. Reig-Viader, G. Gou, D. Goulding, A. Izquierdo, J. S. Choudhary, R. D. Emes, S. G. N. Grant, Evolution of complexity in the zebrafish synapse proteome. *Nat. Commun.* **8**, 14613 (2017).
38. B. C. Carlyle *et al.*, Multiplexed fractionated proteomics reveals synaptic factors associated with cognitive resilience in Alzheimer's disease. bioRxiv 2020.07.31.230680 [Preprint]. 1 August 2020. https://doi.org/10.1101/2020.07.31.230680.
39. J. Choi, M. C. Sullards, J. A. Olzmann, H. D. Rees, S. T. Weintraub, D. E. Bostwick, M. Gearing, A. I. Levey, L. S. Chin, L. Li, Oxidative damage of DJ-1 is linked to sporadic Parkinson and Alzheimer diseases. *J. Biol. Chem.* **281**, 10816–10824 (2006).
40. K. Solti, W. L. Kuan, B. Fórizs, G. Kustos, J. Mihály, Z. Varga, B. Herberth, É. Moravcsik, R. Kiss, M. Kárpáti, A. Mikes, Y. Zhao, T. Imre, J. C. Rochet, F. Aigbirhio, C. H. Williams-Gray, R. A. Barker, G. Tóth, DJ-1 can form β-sheet structured aggregates that co-localize with pathological amyloid deposits. *Neurobiol. Dis.* **134**, 104629 (2020).
41. D. J. Moore, L. Zhang, J. Troncoso, M. K. Lee, N. Hattori, Y. Mizuno, T. M. Dawson, V. L. Dawson, Association of DJ-1 and parkin mediated by pathogenic DJ-1 mutations and oxidative stress. *Hum. Mol. Genet.* **14**, 71–84 (2005).
42. P. Heutink, PINK-1 and DJ-1—New genes for autosomal recessive Parkinson's disease. *J. Neural Transm. Suppl.* **2006**, 215–219 (2006).
43. T. J. Montine, K. S. Montine, W. McMahan, W. R. Markesbery, J. F. Quinn, J. D. Morrow, F2-isoprostanes in Alzheimer and other neurodegenerative diseases. *Antioxid. Redox Signal.* **7**, 269–275 (2005).
44. H. Ohnishi, Y. Kaneko, H. Okazawa, M. Miyashita, R. Sato, A. Hayashi, K. Tada, S. Nagata, M. Takahashi, T. Matozaki, Differential localization of Src homology 2 domain-containing protein tyrosine phosphatase substrate-1 and CD47 and its molecular mechanisms in cultured hippocampal neurons. *J. Neurosci.* **25**, 2702–2711 (2005).
45. A. B. Toth, A. Terauchi, L. Y. Zhang, E. M. Johnson-Venkatesh, D. J. Larsen, M. A. Sutton, H. Umemori, Synapse maturation by activity-dependent ectodomain shedding of SIRPα. *Nat. Neurosci.* **16**, 1417–1425 (2013).
46. T. W. Miller, J. S. Isenberg, H. B. Shih, Y. Wang, D. D. Roberts, Amyloid-β inhibits No-cGMP signaling in a CD36- and CD47-dependent manner. *PLOS ONE* **5**, e15686 (2010).
47. M. H. Han, D. H. Lundgren, S. Jaiswal, M. Chao, K. L. Graham, C. S. Garris, R. C. Axtell, P. P. Ho, C. B. Lock, J. I. Woodard, S. E. Brownell, M. Zoudilova, J. F. V. Hunt, S. E. Baranzini, E. C. Butcher, C. S. Raine, R. A. Sobel, D. K. Han, I. Weissman, L. Steinman, Janus-like opposing roles of CD47 in autoimmune brain inflammation in humans and mice. *J. Exp. Med.* **209**, 1325–1334 (2012).
48. E. K. Lehrman, D. K. Wilton, E. Y. Litvina, C. A. Welsh, S. T. Chang, A. Frouin, A. J. Walker, M. D. Heller, H. Umemori, C. Chen, B. Stevens, CD47 protects synapses from excess microglia-mediated pruning during development. *Neuron* **100**, 120–134.e6 (2018).
49. T. Bartels, S. De Schepper, S. Hong, Microglia modulate neurodegeneration in Alzheimer's and Parkinson's diseases. *Science* **370**, 66–69 (2020).
50. M. P. Chao, C. H. Takimoto, D. D. Feng, K. M. Kenna, P. Gip, J. Liu, J.-P. Volkmer, I. L. Weissman, R. Majeti, Therapeutic targeting of the macrophage immune checkpoint CD47 in myeloid malignancies. *Front. Oncol.* **9**, 1380 (2020).
51. J. D. Ulrich, T. K. Ulland, T. E. Mahan, S. Nyström, K. P. Nilsson, W. M. Song, Y. Zhou, M. Reinartz, S. Choi, H. Jiang, F. R. Stewart, E. Anderson, Y. Wang, M. Colonna, D. M. Holtzman, ApoE facilitates the microglial response to amyloid plaque pathology. *J. Exp. Med.* **215**, 1047–1058 (2018).
52. Y. Shi, K. Yamada, S. A. Liddelow, S. T. Smith, L. Zhao, W. Luo, R. M. Tsai, S. Spina, L. T. Grinberg, J. C. Rojas, G. Gallardo, K. Wang, J. Roh, G. Robinson, M. B. Finn, H. Jiang, P. M. Sullivan, C. Baufeld, M. W. Wood, C. Sutphen, L. M. Cue, C. Xiong, J. L. Del-Aguila, J. C. Morris, C. Cruchaga; Alzheimer's Disease Neuroimaging Initiative, A. M. Fagan, B. L. Miller, A. L. Boxer, W. W. Seeley, O. Butovsky, B. A. Barres, S. M. Paul, D. M. Holtzman, ApoE4 markedly exacerbates tau-mediated neurodegeneration in a mouse model of tauopathy. *Nature* **549**, 523–527 (2017).
53. T.-P. V. Huynh, F. Liao, C. M. Francis, G. O. Robinson, J. R. Serrano, H. Jiang, J. Roh, M. B. Finn, P. M. Sullivan, T. J. Esparza, F. R. Stewart, T. E. Mahan, J. D. Ulrich, T. Cole, D. M. Holtzman, Age-dependent effects of apoE reduction using antisense oligonucleotides in a model of β-amyloidosis. *Neuron* **96**, 1013–1023.e4 (2017).
54. G. M. McKhann, D. S. Knopman, H. Chertkow, B. T. Hyman, C. R. Jack Jr., C. H. Kawas, W. E. Klunk, W. J. Koroshetz, J. J. Manly, R. Mayeux, R. C. Mohs, J. C. Morris, M. N. Rossor, P. Scheltens, M. C. Carrillo, B. Thies, S. Weintraub, C. H. Phelps, The diagnosis of dementia due to Alzheimer's disease: Recommendations from the National Institute on Aging-Alzheimer's Association workgroups on diagnostic guidelines for Alzheimer's disease. *Alzheimers Dement.* **7**, 263–269 (2011).
55. D. R. Bandura, V. I. Baranov, O. I. Ornatsky, A. Antonov, R. Kinach, X. Lou, S. Pavlov, S. Vorobiev, J. E. Dick, S. D. Tanner, Mass cytometry: Technique for real time single cell multitarget immunoassay based on inductively coupled plasma time-of-flight mass spectrometry. *Anal. Chem.* **81**, 6813–6822 (2009).
56. M. Uhlen, A. Bandrowski, S. Carr, A. Edwards, J. Ellenberg, E. Lundberg, D. L. Rimm, H. Rodriguez, T. Hiltke, M. Snyder, T. Yamamoto, A proposal for validation of antibodies. *Nat. Methods* **13**, 823–827 (2016).
57. L. Holcomb, M. N. Gordon, E. McGowan, X. Yu, S. Benkovic, P. Jantzen, K. Wright, I. Saad, R. Mueller, D. Morgan, S. Sanders, C. Zehr, K. O'Campo, J. Hardy, C. M. Prada, C. Eckman, S. Younkin, K. Hsiao, K. Duff, Accelerated Alzheimer-type phenotype in transgenic mice carrying both mutant amyloid precursor protein and presenilin 1 transgenes. *Nat. Med.* **4**, 97–100 (1998).
58. N. Stanley, I. A. Stelzer, A. S. Tsai, R. Fallahzadeh, E. Ganio, M. Becker, T. Phongpreecha, H. Nassar, S. Ghaemi, I. Maric, A. Culos, A. L. Chang, M. Xenochristou, X. Han, C. Espinosa, K. Rumer, L. Peterson, F. Verdonk, D. Gaudilliere, E. Tsai, D. Feyaerts, J. Einhaus, K. Ando, R. J. Wong, G. Obermoser, G. M. Shaw, D. K. Stevenson, M. S. Angst, B. Gaudilliere, N. Aghaeepour, VoPo leverages cellular heterogeneity for predictive modeling of single-cell data. *Nat. Commun.* **11**, 3738 (2020).
59. S. Van Gassen, B. Callebaut, M. J. Van Helden, B. N. Lambrecht, P. Demeester, T. Dhaene, Y. Saeys, FlowSOM: Using self-organizing maps for visualization and interpretation of cytometry data. *Cytometry A* **87**, 636–645 (2015).
60. L. M. Weber, M. D. Robinson, Comparison of clustering methods for high-dimensional single-cell flow and mass cytometry data. *Cytometry A* **89**, 1084–1096 (2016).
61. X. Liu, W. Song, B. Y. Wong, T. Zhang, S. Yu, G. N. Lin, X. Ding, A comparison framework and guideline of clustering methods for mass cytometry data. *Genome Biol.* **20**, 297 (2019).
62. X. Guo, L. Gao, X. Liu, J. Yin, Improved deep embedded clustering with local structure preservation, in *Proceedings of the Twenty-Sixth International Joint Conference on Artificial Intelligence* (IJCAI, 2017), pp. 1753–1759.
63. K. Hornik, A CLUE for CLUster ensembles. *J. Stat. Softw.* **14**, 1–25 (2005).
64. K. H. Gylys, J. A. Fein, G. M. Cole, Quantitative characterization of crude synaptosomal fraction (P-2) components by flow cytometry. *J. Neurosci. Res.* **61**, 186–192 (2000).
65. K. H. Gylys, J. A. Fein, F. Yang, D. J. Wiley, C. A. Miller, G. M. Cole, Synaptic changes in Alzheimer's disease: Increased amyloid-beta and gliosis in surviving terminals is accompanied by decreased PSD-95 fluorescence. *Am. J. Pathol.* **165**, 1809–1817 (2004).
66. A. Culos, A. S. Tsai, N. Stanley, M. Becker, M. S. Ghaemi, D. R. McIlwain, R. Fallahzadeh, A. Tanada, H. Nassar, C. Espinosa, M. Xenochristou, E. Ganio, L. Peterson, X. Han, I. A. Stelzer, K. Ando, D. Gaudilliere, T. Phongpreecha, I. Marić, A. L. Chang, G. M. Shaw, D. K. Stevenson, S. Bendall, K. L. Davis, W. Fantl, G. P. Nolan, T. Hastie, R. Tibshirani, M. S. Angst, B. Gaudilliere, N. Aghaeepour, Integration of mechanistic immunological knowledge into a machine learning pipeline improves predictions. *Nat. Mach. Intell.* **2**, 619–628 (2020).
67. T. Phongpreecha, R. Fernandez, D. Mrdjen, A. Culos, C. R. Gajera, A. M. Wawro, N. Stanley, B. Gaudilliere, K. L. Poston, N. Aghaeepour, T. J. Montine, Single-cell peripheral immunoprofiling of Alzheimer's and Parkinson's diseases. *Sci. Adv.* **6**, eabd5575 (2020).
68. M. M. B. Bosse, S. C. Bendall, M. R. Angelo, MIBI staining: Human BioMolecular Atlas Program (HuBMAP) Method Development Community. protocols.io. 2021 (dx.doi.org/10.17504/protocols.io.bt9tnr6n).
69. M. M. B. Bosse, S. C. Camacho, S. C. Bendall, M. R. Angelo, MIBI and IHC solutions: Human BioMolecular Atlas Program (HuBMAP) Method Development Community. protocols.io. 2021 (dx.doi.org/10.17504/protocols.io.bhmej43e).
70. M. Traka, J. R. Podojil, D. P. McCarthy, S. D. Miller, B. Popko, Oligodendrocyte death results in immune-mediated CNS demyelination. *Nat. Neurosci.* **19**, 65–74 (2016).
71. T. Barron, J. Saifetiarova, M. A. Bhat, J. H. Kim, Myelination of Purkinje axons is critical for resilient synaptic transmission in the deep cerebellar nucleus. *Sci. Rep.* **8**, 1022 (2018).
72. J. M. Boggs, L. Homchaudhuri, G. Ranagaraj, Y. Liu, G. S. T. Smith, G. Harauz, Interaction of myelin basic protein with cytoskeletal and signaling proteins in cultured primary oligodendrocytes and N19 oligodendroglial cells. *BMC Res. Notes* **7**, 387 (2014).
73. R. R. Voskuhl, T. M. Pribyl, K. Kampf, V. Handley, H. B. Liu, J. M. Feng, C. W. Campagnoni, S. S. Soldan, A. Messing, A. T. Campagnoni, Experimental autoimmune encephalomyelitis relapses are reduced in heterozygous golli MBP knockout mice. *J. Neuroimmunol.* **139**, 44–50 (2003).
74. E. M. Treutlein, K. Kern, A. Weigert, N. Tarighi, C. D. Schuh, R. M. Nüsing, Y. Schreiber, N. Ferreirós, B. Brüne, G. Geisslinger, S. Pierre, K. Scholich, The prostaglandin E2 receptor EP3 controls CC-chemokine ligand 2-mediated neuropathic pain induced by mechanical nerve damage. *J. Biol. Chem.* **293**, 9685–9695 (2018).
75. L. C. Tafoya, M. Mameli, T. Miyashita, J. F. Guzowski, C. F. Valenzuela, M. C. Wilson, Expression and function of SNAP-25 as a universal SNARE component in GABAergic neurons. *J. Neurosci.* **26**, 7826–7838 (2006).
76. N. O. Postupna, C. D. Keene, C. Latimer, E. E. Sherfield, R. D. van Gelder, J. G. Ojemann, T. J. Montine, M. Darvas, Flow cytometry analysis of synaptosomes from post-mortem human brain reveals changes specific to Lewy body and Alzheimer's disease. *Lab. Investig.* **94**, 1161–1172 (2014).
77. S. Won, S. Incontro, R. A. Nicoll, K. W. Roche, PSD-95 stabilizes NMDA receptors by inducing the degradation of STEP61. *Proc. Natl. Acad. Sci. U.S.A.* **113**, E4736–E4744 (2016).
78. S. R. Gordon, R. L. Maute, B. W. Dulken, G. Hutter, B. M. George, M. N. McCracken, R. Gupta, J. M. Tsai, R. Sinha, D. Corey, A. M. Ring, A. J. Connolly, I. L. Weissman, PD-1 expression by

tumour-associated macrophages inhibits phagocytosis and tumour immunity. *Nature* **545**, 495–499 (2017).
79. Y. Kojima, J. P. Volkmer, K. McKenna, M. Civelek, A. J. Lusis, C. L. Miller, D. Direnzo, V. Nanda, J. Ye, A. J. Connolly, E. E. Schadt, T. Quertermous, P. Betancur, L. Maegdefessel, L. P. Matic, U. Hedin, I. L. Weissman, N. J. Leeper, CD47-blocking antibodies restore phagocytosis and prevent atherosclerosis. *Nature* **536**, 86–90 (2016).
80. S. B. Willingham, J. P. Volkmer, A. J. Gentles, D. Sahoo, P. Dalerba, S. S. Mitra, J. Wang, H. Contreras-Trujillo, R. Martin, J. D. Cohen, P. Lovelace, F. A. Scheeren, M. P. Chao, K. Weiskopf, C. Tang, A. K. Volkmer, T. J. Naik, T. A. Storm, A. R. Mosley, B. Edris, S. M. Schmid, C. K. Sun, M. S. Chua, O. Murillo, P. Rajendran, A. C. Cha, R. K. Chin, D. Kim, M. Adorno, T. Raveh, D. Tseng, S. Jaiswal, P. O. Enger, G. K. Steinberg, G. Li, S. K. So, R. Majeti, G. R. Harsh, M. van de Rijn, N. N. H. Teng, J. B. Sunwoo, A. A. Alizadeh, M. F. Clarke, I. L. Weissman, The CD47-signal regulatory protein alpha (SIRPa) interaction is a therapeutic target for human solid tumors. *Proc. Natl. Acad. Sci. U.S.A.* **109**, 6662–6667 (2012).
81. A. Ashok, S. Karmakar, R. Chandel, R. Ravikumar, S. Dalal, Q. Kong, N. Singh, Prion protein modulates iron transport in the anterior segment: Implications for ocular iron homeostasis and prion transmission. *Exp. Eye Res.* **175**, 1–13 (2018).
82. C. Lund, C. M. Olsen, H. Tveit, M. A. Tranulis, Characterization of the prion protein 3F4 epitope and its use as a molecular tag. *J. Neurosci. Methods* **165**, 183–190 (2007).
83. R. J. Kascsak, R. Rubenstein, P. A. Merz, M. Tonna-DeMasi, R. Fersko, R. I. Carp, H. M. Wisniewski, H. Diringer, Mouse polyclonal and monoclonal antibody to scrapie-associated fibril proteins. *J. Virol.* **61**, 3688–3693 (1987).
84. S. Gilch, M. Nunziante, A. Ertmer, F. Wopfner, L. Laszlo, H. M. Schätzl, Recognition of lumenal prion protein aggregates by post-ER quality control mechanisms is mediated by the preoctarepeat region of PrP. *Traffic* **5**, 300–313 (2004).
85. S. V. Yelamanchili, G. Pendyala, I. Brunk, M. Darna, U. Albrecht, G. Ahnert-Hilger, Differential sorting of the vesicular glutamate transporter 1 into a defined vesicular pool is regulated by light signaling involving the clock gene Period2. *J. Biol. Chem.* **281**, 15671–15679 (2006).
86. H. Dimant, L. Zhu, L. N. Kibuuka, Z. Fan, B. T. Hyman, P. J. McLean, Direct visualization of CHIP-mediated degradation of alpha-synuclein in vivo: Implications for PD therapeutics. *PLOS ONE* **9**, e92098 (2014).
87. M. E. Larson, M. A. Sherman, S. Greimel, M. Kuskowski, J. A. Schneider, D. A. Bennett, S. E. Lesne, Soluble α-synuclein is a novel modulator of Alzheimer's disease pathophysiology. *J. Neurosci.* **32**, 10253–10266 (2012).
88. R. Jakes, R. A. Crowther, V. M. Y. Lee, J. Q. Trojanowski, T. Iwatsubo, M. Goedert, Epitope mapping of LB509, a monoclonal antibody directed against human alpha-synuclein. *Neurosci. Lett.* **269**, 13–16 (1999).
89. M. Fernández-Nogales, M. Santos-Galindo, J. Merchán-Rubira, J. J. M. Hoozemans, A. Rábano, I. Ferrer, J. Avila, F. Hernández, J. J. Lucas, Tau-positive nuclear indentations in P301S tauopathy mice. *Brain Pathol.* **27**, 314–322 (2017).
90. M. Demars, Y. S. Hu, A. Gadadhar, O. Lazarov, Impaired neurogenesis is an early event in the etiology of familial Alzheimer's disease in transgenic mice. *J. Neurosci. Res.* **88**, 2103–2117 (2010).
91. D. M. Wilcock, M. R. Lewis, W. E. van Nostrand, J. Davis, M. L. Previti, N. Gharkholonarehe, M. P. Vitek, C. A. Colton, Progression of amyloid pathology to Alzheimer's disease pathology in an amyloid precursor protein transgenic mouse model by removal of nitric oxide synthase 2. *J. Neurosci.* **28**, 1537–1545 (2008).
92. S. A. Austin, M. A. Sens, C. K. Combs, Amyloid precursor protein mediates a tyrosine kinase-dependent activation response in endothelial cells. *J. Neurosci.* **29**, 14451–14462 (2009).
93. J. M. Ramaker, T. L. Swanson, P. F. Copenhaver, Amyloid precursor proteins interact with the heterotrimeric G protein Go in the control of neuronal migration. *J. Neurosci.* **33**, 10165–10181 (2013).
94. C. Hilbich, U. Mönning, C. Grund, C. L. Masters, K. Beyreuther, Amyloid-like properties of peptides flanking the epitope of amyloid precursor protein-specific monoclonal antibody 22C11. *J. Biol. Chem.* **268**, 26571–26577 (1993).
95. S. F. Kash, R. S. Johnson, L. H. Tecott, J. L. Noebels, R. D. Mayfield, D. Hanahan, S. Baekkeskov, Epilepsy in mice deficient in the 65-kDa isoform of glutamic acid decarboxylase. *Proc. Natl. Acad. Sci. U.S.A.* **94**, 14060–14065 (1997).
96. M. G. Erlander, N. J. Tillakaratne, S. Feldblum, N. Patel, A. J. Tobin, Two genes encode distinct glutamate decarboxylases. *Neuron* **7**, 91–100 (1991).
97. S. Feldblum, M. G. Erlander, A. J. Tobin, Different distributions of GAD65 and GAD67 mRNAs suggest that the two glutamate decarboxylases play distinctive functional roles. *J. Neurosci. Res.* **34**, 689–706 (1993).
98. Y. C. Chang, D. I. Gottlieb, Characterization of the proteins purified with monoclonal antibodies to glutamic acid decarboxylase. *J. Neurosci.* **8**, 2123–2130 (1988).
99. S. D. Blasio, I. M. N. Wortel, D. A. G. van Bladel, L. E. de Vries, T. D.-d. Boer, K. Worah, N. de Haas, S. I. Buschow, I. J. M. de Vries, C. G. Figdor, S. V. Hato, Human CD1c(+) DCs are critical cellular mediators of immune responses induced by immunogenic cell death. *Oncoimmunology* **5**, e1192739 (2016).
100. M. Feng, K. D. Marjon, F. Zhu, R. Weissman-Tsukamoto, A. Levett, K. Sullivan, K. S. Kao, M. Markovic, P. A. Bump, H. M. Jackson, T. S. Choi, J. Chen, A. M. Banuelos, J. Liu, P. Gip, L. Cheng, D. Wang, I. L. Weissman, Programmed cell removal by calreticulin in tissue homeostasis and cancer. *Nat. Commun.* **9**, 3194 (2018).
101. C. W. Chang, C. W. Chiang, J. D. Gaffaney, E. R. Chapman, M. B. Jackson, Lipid-anchored synaptobrevin provides little or no support for exocytosis or liposome fusion. *J. Biol. Chem.* **291**, 2848–2857 (2016).
102. S. Schoch, F. Deák, A. Königstorfer, M. Mozhayeva, Y. Sara, T. C. Südhof, E. T. Kavalali, SNARE function analyzed in synaptobrevin/VAMP knockout mice. *Science* **294**, 1117–1122 (2001).
103. J. N. K. Nyarko, M. O. Quartey, R. M. Heistad, P. R. Pennington, L. J. Poon, K. J. Knudsen, O. Allonby, A. M. el Zawily, A. Freywald, G. Rauw, G. B. Baker, D. D. Mousseau, Glycosylation states of pre- and post-synaptic markers of 5-HT neurons differ with sex and 5-HTTLPR genotype in cortical autopsy samples. *Front. Neurosci.* **12**, 545 (2018).
104. Q. Zhou, A. Yen, G. Rymarczyk, H. Asai, C. Trengrove, N. Aziz, M. T. Kirber, G. Mostoslavsky, T. Ikezu, B. Wolozin, V. M. Bolotina, Impairment of PARK14-dependent Ca(2+) signalling is a novel determinant of Parkinson's disease. *Nat. Commun.* **7**, 10332 (2016).
105. C. I. Maeder, J.-I. Kim, X. Liang, K. Kaganovsky, A. Shen, Q. Li, Z. Li, S. Wang, X. Z. S. Xu, J. B. Li, Y. K. Xiang, J. B. Ding, K. Shen, The THO complex coordinates transcripts for synapse development and dopamine neuron survival. *Cell* **174**, 1436–1449.e20 (2018).
106. J. C. Watts, C. Condello, J. Stohr, A. Oehler, J. Lee, S. J. DeArmond, L. Lannfelt, M. Ingelsson, K. Giles, S. B. Prusiner, Serial propagation of distinct strains of Aβ prions from Alzheimer's disease patients. *Proc. Natl. Acad. Sci. U.S.A.* **111**, 10323–10328 (2014).
107. J. S. Miners, J. C. Palmer, S. Love, Pathophysiology of hypoperfusion of the precuneus in early Alzheimer's disease. *Brain Pathol.* **26**, 533–541 (2016).
108. A. K. Clippinger, S. D'Alton, W. L. Lin, T. F. Gendron, J. Howard, D. R. Borchelt, A. Cannon, Y. Carlomagno, P. Chakrabarty, C. Cook, T. E. Golde, Y. Levites, L. Ranum, P. J. Schultheis, G. Xu, L. Petrucelli, N. Sahara, D. W. Dickson, B. Giasson, J. Lewis, Robust cytoplasmic accumulation of phosphorylated TDP-43 in transgenic models of tauopathy. *Acta Neuropathol.* **126**, 39–50 (2013).
109. W. Luo, F. Dou, A. Rodina, S. Chip, J. Kim, Q. Zhao, K. Moulick, J. Aguirre, N. Wu, P. Greengard, G. Chiosis, Roles of heat-shock protein 90 in maintaining and facilitating the neurodegenerative phenotype in tauopathies. *Proc. Natl. Acad. Sci. U.S.A.* **104**, 9511–9516 (2007).
110. C. A. Colton, M. P. Vitek, D. A. Wink, Q. Xu, V. Cantillana, M. L. Previti, W. E. van Nostrand, J. B. Weinberg, H. Dawson, NO synthase 2 (NOS2) deletion promotes multiple pathologies in a mouse model of Alzheimer's disease. *Proc. Natl. Acad. Sci. U.S.A.* **103**, 12867–12872 (2006).
111. A. Yuan, A. Kumar, C. Peterhoff, K. Duff, R. A. Nixon, Axonal transport rates in vivo are unaffected by tau deletion or overexpression in mice. *J. Neurosci.* **28**, 1682–1687 (2008).
112. N. S. Gandhi, I. Landrieu, C. Byrne, P. Kukic, L. Amniai, F. X. Cantrelle, J. M. Wieruszeski, R. L. Mancera, Y. Jacquot, G. Lippens, A phosphorylation-induced turn defines the Alzheimer's disease AT8 antibody epitope on the tau protein. *Angew. Chem. Int. Ed. Engl.* **54**, 6819–6823 (2015).
113. K. Ando, A. Maruko-Otake, Y. Ohtake, M. Hayashishita, M. Sekiya, K. M. Iijima, Stabilization of microtubule-unbound tau via tau phosphorylation at Ser262/356 by Par-1/MARK contributes to augmentation of AD-related phosphorylation and Aβ42-induced tau toxicity. *PLOS Genet.* **12**, e1005917 (2016).
114. T. Bilousova, M. Melnik, E. Miyoshi, B. L. Gonzalez, W. W. Poon, H. V. Vinters, C. A. Miller, M. M. Corrada, C. Kawas, A. Hatami, R. Albay III, C. Glabe, K. H. Gylys, Apolipoprotein E/Amyloid-β complex accumulates in alzheimer disease cortical synapses via apolipoprotein E receptors and is enhanced by APOE4. *Am. J. Pathol.* **189**, 1621–1636 (2019).
115. A. McQuade, Y. J. Kang, J. Hasselmann, A. Jairaman, A. Sotelo, M. Coburn, S. K. Shabestari, J. P. Chadarevian, G. Fote, C. H. Tu, E. Danhash, J. Silva, E. Martinez, C. Cotman, G. A. Prieto, L. M. Thompson, J. S. Steffan, I. Smith, H. Davtyan, M. Cahalan, H. Cho, M. Blurton-Jones, Gene expression and functional deficits underlie TREM2-knockout microglia responses in human models of Alzheimer's disease. *Nat. Commun.* **11**, 5370 (2020).
116. S. L. Siedlak, Y. Jiang, M. L. Huntley, L. Wang, J. Gao, F. Xie, J. Liu, B. Su, G. Perry, X. Wang, TMEM230 accumulation in granulovacuolar degeneration bodies and dystrophic neurites of Alzheimer's disease. *J. Alzheimers Dis.* **58**, 1027–1033 (2017).
117. P. Davies, K. M. Hinkle, N. N. Sukar, B. Sepulveda, R. Mesias, G. Serrano, D. R. Alessi, T. G. Beach, D. L. Benson, C. L. White III, R. M. Cowell, S. S. Das, A. B. West, H. L. Melrose, Comprehensive characterization and optimization of anti-LRRK2 (leucine-rich repeat kinase 2) monoclonal antibodies. *Biochem. J.* **453**, 101–113 (2013).
118. E. J. Bae, N. Y. Yang, M. Song, C. S. Lee, J. S. Lee, B. C. Jung, H. J. Lee, S. Kim, E. Masliah, S. P. Sardi, S. J. Lee, Glucocerebrosidase depletion enhances cell-to-cell transmission of α-synuclein. *Nat. Commun.* **5**, 4755 (2014).
119. S. P. Tay, C. W. S. Yeo, C. Chai, P. J. Chua, H. M. Tan, A. X. Y. Ang, D. L. H. Yip, J. X. Sung, P. H. Tan, B. H. Bay, S. H. Wong, C. Tang, J. M. M. Tan, K. L. Lim, Parkin enhances

the expression of cyclin-dependent kinase 6 and negatively regulates the proliferation of breast cancer cells. *J. Biol. Chem.* **285**, 29231–29238 (2010).
120. J. W. Jin, X. Fan, E. del Cid-Pellitero, X. X. Liu, L. Zhou, C. Dai, E. Gibbs, W. He, H. Li, X. Wu, A. Hill, B. R. Leavitt, N. Cashman, L. Liu, J. Lu, T. M. Durcan, Z. Dong, E. A. Fon, Y. T. Wang, Development of an α-synuclein knockdown peptide and evaluation of its efficacy in Parkinson's disease models. *Commun. Biol.* **4**, 232 (2021).
121. Y. Ruan, K. Hu, H. Chen, Autophagy inhibition enhances isorhamnetin-induced mitochondria-dependent apoptosis in non-small cell lung cancer cells. *Mol. Med. Rep.* **12**, 5796–5806 (2015).
122. J. P. Gaut, J. Byun, H. D. Tran, W. M. Lauber, J. A. Carroll, R. S. Hotchkiss, A. Belaaouaj, J. W. Heinecke, Myeloperoxidase produces nitrating oxidants in vivo. *J. Clin. Invest.* **109**, 1311–1319 (2002).
123. M. Dhiman, E. S. Nakayasu, Y. H. Madaiah, B. K. Reynolds, J. J. Wen, I. C. Almeida, N. J. Garg, Enhanced nitrosative stress during Trypanosoma cruzi infection causes nitrotyrosine modification of host proteins: Implications in Chagas' disease. *Am. J. Pathol.* **173**, 728–740 (2008).
124. A. Venkatesan, L. Uzasci, Z. Chen, L. Rajbhandari, C. Anderson, M. H. Lee, M. A. Bianchet, R. Cotter, H. Song, A. Nath, Impairment of adult hippocampal neural progenitor proliferation by methamphetamine: Role for nitrotyrosination. *Mol. Brain* **4**, 28 (2011).
125. K. Newton, M. L. Matsumoto, I. E. Wertz, D. S. Kirkpatrick, J. R. Lill, J. Tan, D. Dugger, N. Gordon, S. S. Sidhu, F. A. Fellouse, L. Komuves, D. M. French, R. E. Ferrando, C. Lam, D. Compaan, C. Yu, I. Bosanac, S. G. Hymowitz, R. F. Kelley, V. M. Dixit, Ubiquitin chain editing revealed by polyubiquitin linkage-specific antibodies. *Cell* **134**, 668–678 (2008).
126. J. V. Ferreira, A. R. Soares, J. S. Ramalho, P. Pereira, H. Girao, K63 linked ubiquitin chain formation is a signal for HIF1A degradation by chaperone-mediated autophagy. *Sci. Rep.* **5**, 10210 (2015).
127. M. H. Chen, T. L. Hagemann, R. A. Quinlan, A. Messing, M. D. Perng, Caspase cleavage of GFAP produces an assembly-compromised proteolytic fragment that promotes filament aggregation. *ASN Neuro* **5**, e00125 (2013).
128. Y. S. Chen, S. C. Lim, M. H. Chen, R. A. Quinlan, M. D. Perng, Alexander disease causing mutations in the C-terminal domain of GFAP are deleterious both to assembly and network formation with the potential to both activate caspase 3 and decrease cell viability. *Exp. Cell Res.* **317**, 2252–2266 (2011).
129. S. A. Baker, C. R. Gajera, A. M. Wawro, M. R. Corces, T. J. Montine, GATM and GAMT synthesize creatine locally throughout the mammalian body and within oligodendrocytes of the brain. *Brain Res.* **1770**, 147627 (2021).
130. A. M. Wawro, C. R. Gajera, S. A. Baker, J. J. Nirschl, H. Vogel, T. J. Montine, Creatine transport and pathological changes in creatine transporter deficient mice. *J. Inherit. Metab. Dis.* **44**, 939–948 (2021).

Acknowledgments: We thank K. I. Andreasson for providing PS/APP mice. **Funding:** This work was supported by NIH grants AG057707 (T.J.M.), R35GM138353 (N.A.), HL087103 (C.A.S.), AG058829 (C.A.S. and S.C.), AG049638 (S.C.), HL122393 (T.C.R.), AG057915 (S.C.B.), AG056287 (S.C.B.), AG068279 (S.C.B.), P30 AG066515 (V. Henderson), and P30 AG066509 (T. Grabowski).
Author contributions: Conceptualization: T.J.M., N.A., S.C.B., C.R.G., and T.P. Resources: N.P., E.S., C.L., C.A.S., T.C.R., S.C., K.L.P., and C.D.K. Methodology: C.R.G., R.Fe., T.P., C.C.L., A.L.C., M.B., R.Fa., K.V., T.J.M., N.A., S.C.B., and M.A. Investigation: C.R.G., R.Fe., and K.V. Software: T.P., C.C.L., A.L.C., M.B., D.T., and R.Fa. Visualization: T.P., T.J.M., C.C.L., K.V., and K.S.M. Funding acquisition: T.J.M., N.A., C.A.S., S.C., T.C.R., K.S.P., and E.J.F. Project administration: T.J.M. and T.P. Supervision: T.J.M. Writing—original draft: T.J.M., T.P., C.R.G., C.C.L., and K.V. Writing—review and editing: N.A., S.C.B., M.A., C.D.K., K.L.P., E.J.F., K.S.M., S.C., C.A.S., A.L.C., M.B., R.Fa., and N.P. **Competing interests:** K.L.P. has received consulting fees and stock options from Curasen. S.C.B. is one of the inventors on a MIBI technology related to this work filed by Stanford University (no. US2015/0080233A1, filed on 11 September 2014, published on 19 March 2015). He is also a board member, shareholder, and consultant in Ionpath Inc. Other authors declare that they have no competing interests. **Data and materials availability:** Both human and mice single-synapse data, and the codes for clustering and subsequent analysis, are available on Dryad at https://doi.org/10.5061/dryad.z612jm6cr. The codes are also available at https://github.com/tpjoe/SynTOF2021.

Submitted 18 June 2021
Accepted 28 October 2021
Published 15 December 2021
10.1126/sciadv.abk0473